Chapter 4
Time-Delayed Feedback Control: From Simple Models to Lasers and Neural Systems

Eckehard Schöll, Philipp Hövel, Valentin Flunkert, and Markus A. Dahlem

4.1 Introduction

Over the past decade control of unstable states has evolved into a central issue in applied nonlinear science [1]. This field has various aspects comprising stabilization of unstable periodic orbits embedded in a deterministic chaotic attractor, which is generally referred to as *chaos control*, stabilization of unstable fixed points (steady states), or control of the coherence and timescales of stochastic motion. Various methods of control, going well beyond the classical control theory [2–4], have been developed since the ground-breaking work of Ott, Grebogi, and Yorke [5] in which they demonstrated that small time dependent changes in the control parameters of a nonlinear system can turn a previously chaotic trajectory into a stable periodic motion. One scheme where the control force is constructed from time-delayed signals [6] has turned out to be very robust and universal to apply and easy to implement experimentally. It has been used in a large variety of systems in physics, chemistry, biology, medicine, and engineering [1, 7, 8], in purely temporal dynamics as well as in spatially extended systems [9–25]. Moreover, it has recently been shown to be applicable also to noise-induced oscillations and patterns [26–29]. This is an interesting observation in the context of ongoing research on the constructive influence of noise in nonlinear systems [30–35].

In time-delayed feedback control (*time-delay autosynchronization* or TDAS) the control signal is built from the difference $s(t) - s(t - \tau)$ between the present and an earlier value of an appropriate system variable s. It is *non-invasive* since the control forces vanish if the target state (a periodic state of period τ or a steady state) is reached. Thus the unstable states themselves of the uncontrolled system are not changed, but only their neighborhood is adjusted such that neighboring trajectories converge to it, i.e., the control forces act only if the system deviates from the state to be stabilized. Involving no numerically expensive computations, time-delayed

E. Schöll (✉)
Institut für Theoretische Physik, Technische Universität Berlin, Hardenbergstraße 36, 10623 Berlin, Germany
e-mail: schoell@physik.tu-berlin.de

F.M. Atay (ed.), *Complex Time-Delay Systems,* Understanding Complex Systems,
DOI 10.1007/978-3-642-02329-3_4,

feedback control is capable of controlling systems with very fast dynamics still in real-time mode [36–38]. Moreover, detailed knowledge of the target state is not required.

An extension to multiple time delays has been proposed by Socolar et al. [39], who considered multiple delays in form of an infinite series (ETDAS) or an average of N past iterates (*N time-delay autosynchronization* or NTDAS) [40] or coupling matrices (*generalized ETDAS* or GETDAS) [41]. Analytical insight into those schemes has been obtained by several theoretical studies, e.g., [42–54] as well as by numerical bifurcation analysis, e.g., [55, 56]. Time-delayed feedback can also stabilize fixed points using single [48, 49, 57] or multiple delay times [50, 58, 59]. The efficiency of these schemes can be improved by deterministic or stochastic modulation of the time delay [60].

Recent work has focused, on the one hand, on basic aspects like developing novel control schemes and gaining analytical insights, and on the other hand, on applications to optical and electronic systems, including laser diodes, electronic circuits, and semiconductor nanostructures [18, 61, 62], to chemical and electrochemical reaction systems [15, 16, 63–70], and to biological and medical systems, including the suppression of synchronization as therapeutic tools for neural diseases like Parkinson and epilepsy [71, 72], and control of cardiac dynamics [73]. In particular, networks of oscillatory or excitable elements, e.g., neural networks or coupled laser arrays, have been considered, where time delays naturally arise through signal propagation and processing times [74–82]. Systems composed of a small number of coupled oscillatory or excitable elements (lasers or neurons) can be conceived as network motifs of larger networks. Time-delayed feedback control schemes with different couplings of the control force have been applied to various models of nonlinear semiconductor oscillators, e.g., impact ionization-driven Hall instability [83], and semiconductor nanostructures described by an N-shaped [14, 84, 85], S-shaped [9, 11, 12, 24, 86], or Z-shaped [13] current-field characteristics. In semiconductor nanostructures complex chaotic spatio-temporal field and current patterns arise in the form of traveling field domains (for the N type) and breathing or spiking current filaments (for the S and Z types), which can be stabilized by time-delayed feedback control.

Time-delayed feedback control has also been applied to purely noise-induced oscillations and patterns in a regime where the deterministic system rests in a steady state, and in this way both the coherence and the mean frequency of the oscillations have been controlled in various nonlinear systems [26–28, 87–91], including chemical systems [92], neural systems [93, 94], laser diodes [95], and semiconductor nanostructures of N type [96–99] and Z type [100–102]. The control of deterministic and stochastic spatio-temporal patterns in semiconductor nanostructures by time-delayed feedback is reviewed elsewhere [62].

In this review we focus on simple models, for which some analytical results can be obtained in addition to computer simulations, and apply them to a selection of systems ranging from semiconductor lasers to neurosystems. We will show that time-delayed feedback control methods have a wider range of applicability than previously assumed, when applied to unstable steady states and to unstable periodic

orbits, using generic normal forms. In the case of unstable periodic orbits the often invoked *odd number limitation*, which had been believed to impose serious restrictions for a long time, has recently been refuted [52]. Further, we will discuss applications to lasers and coupled neural systems in the framework of the Lang–Kobayashi laser model and the FitzHugh–Nagumo neuron model. We will demonstrate the suppression and enhancement of synchronization by time-delayed feedback, and point out some complex scenarios of synchronized in-phase or antiphase oscillations, bursting patterns, or amplitude death, induced by delayed coupling in combination with delayed feedback in simple network motifs.

4.2 Time-Delayed Feedback Control of Generic Systems

In this section we review basic properties of time-delayed feedback control, using simple normal form models which are representative of a large class of nonlinear dynamic systems [48–50, 52, 54].

4.2.1 Stabilization of Unstable Steady States

Time-delayed feedback methods, which have originally been used to control unstable periodic orbits [6], provide also a tool to stabilize unstable steady states [57, 103, 58, 59, 48–50, 60]. We present a numerical and analytical investigations of the feedback scheme using the Lambert function and discuss the extension to multiple time feedback control (ETDAS).

Other methods to control unstable steady states use the derivative of the current state as source of a control force [104]. It can be shown, however, that this *derivative control* is sensitive to high-frequency oscillations [105] and thus not robust in the presence of noise. Another control scheme calculates the difference of the current state to a low-pass filtered version [106].

Here we consider a general dynamic system given by a vector field $\mathbf{f}$ [48]:

$$\dot{\mathbf{x}} = \mathbf{f}(\mathbf{x}) \tag{4.1}$$

with an unstable fixed point $\mathbf{x}^* \in \mathbb{R}^n$ given by $\mathbf{f}(\mathbf{x}^*) = 0$. The stability of this fixed point is obtained by linearizing the vector field around $\mathbf{x}^*$. Without loss of generality, let us assume $\mathbf{x}^* = 0$. In the following we will consider the generic case of an unstable focus for which the linearized equations in center manifold coordinates x, y can be written as

$$\begin{aligned} \dot{x} &= \lambda\, x + \omega\, y \\ \dot{y} &= -\omega\, x + \lambda\, y, \end{aligned} \tag{4.2}$$

where λ and ω are positive real numbers. They may be viewed as parameters governing the distance from the instability threshold, e.g., a Hopf bifurcation of system

(4.1), and the intrinsic eigenfrequency, respectively. For notational convenience, (4.2) can be rewritten as

$$\dot{\mathbf{x}}(t) = \mathbf{A}\mathbf{x}(t). \tag{4.3}$$

Alternatively, the components of $\mathbf{x}(t)$ can be understood as real and imaginary parts of a complex variable $z(t) = x(t) + iy(t)$ so that (4.2) reads $\dot{z}(t) = (\lambda + i\omega)z(t)$. The eigenvalues Λ_0 of the matrix $\mathbf{A}$ are given by $\Lambda_0 = \lambda \pm i\omega$, so that for $\lambda > 0$ and $\omega \neq 0$ the fixed point is indeed an unstable focus.

We shall now apply time-delayed feedback control [6] in order to stabilize this fixed point:

$$\dot{\mathbf{x}}(t) = \mathbf{A}\mathbf{x}(t) - \mathbf{F}(t), \tag{4.4}$$

where $\mathbf{F}$ denotes the control force given by

$$\mathbf{F}(t) = K[\mathbf{x}(t) - \mathbf{x}(t-\tau)], \tag{4.5}$$

with the feedback gain $K \in \mathbb{R}$ and the time delay $\tau > 0$. In components this yields

$$\begin{aligned} \dot{x}(t) &= \lambda\, x(t) + \omega\, y(t) - K[x(t) - x(t-\tau)] \\ \dot{y}(t) &= -\omega\, x(t) + \lambda\, y(t) - K[y(t) - y(t-\tau)]. \end{aligned} \tag{4.6}$$

The goal of the control method is to change the sign of the real part of the eigenvalue. Figure 4.1 depicts a schematic diagram of the time-delayed feedback loop. The red color shows the extension of the original Pyragas control including multiple delays (ETDAS) which will be discussed later on.

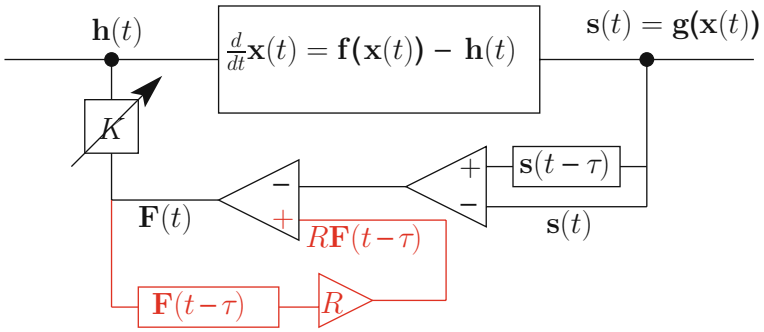

Fig. 4.1 Diagram of the time-delay autosynchronization method. $\mathbf{x}(t)$ denotes the state of the system at time t, $\mathbf{s}(t)$ is the control signal, i.e., some component of $\mathbf{x}(t)$ measured by $\mathbf{g}(\mathbf{x}(t))$, and $\mathbf{F}(t)$ is the control force. The real constants τ, K, and R denote the time delay, the feedback gain, and the memory parameter, respectively. The function $\mathbf{h}(t)$ describes the coupling of $\mathbf{F}$ to the dynamical system $\mathbf{x}$. The extension of the original time-delayed feedback [6] as introduced by Socolar et al. (see [39], ETDAS) is shown in *red color*

Since the control force applied to the *i*th component of the system involves only the same component, this control scheme is called *diagonal coupling* [11], which is suitable for an analytical treatment. Note that the feedback term vanishes if the unstable steady state is stabilized since $x^*(t-\tau) = x^*(t)$ and $y^*(t-\tau) = y^*(t)$ for all t, indicating the non-invasiveness of the TDAS method.

Figure 4.2 depicts the dynamics of the controlled unstable focus ($\lambda = 0.5$ and $\omega = \pi$) in the (x, y) plane for different values of the feedback gain K. Panels (a) through (d) correspond to increasing K. The time delay of the TDAS control scheme is chosen as $\tau = 1$ in all panels. Panel (a) displays the case of the absence of control, i.e., $K = 0$, and shows that the system is an unstable focus exhibiting undamped oscillations on a timescale $T_0 \equiv 2\pi/\omega = 2$. It can be seen from panel (b) that increasing K reduces the instability. The system diverges more slowly to infinity indicated by the tighter spiral. Further increase of K stops the unstable behavior completely and produces periodic motion, i.e., a center [see panel (c)]. The amplitude of the orbit depends on the initial conditions, which are chosen as $x = 0.01$ and $y = 0.01$. For even larger feedback gains, the trajectory becomes an inward spiral and thus approaches the fixed point, i.e., the focus. Hence the TDAS control scheme is successful.

An exponential ansatz for $x(t)$ and $y(t)$ in (4.6), i.e., $x(t) \sim \exp(\Lambda t)$ and $y(t) \sim \exp(\Lambda t)$, reveals how the control force modifies the eigenvalues of the system. The characteristic equation becomes

$$[\Lambda + K\left(1 - e^{-\Lambda\tau}\right) - \lambda]^2 + \omega^2 = 0, \tag{4.7}$$

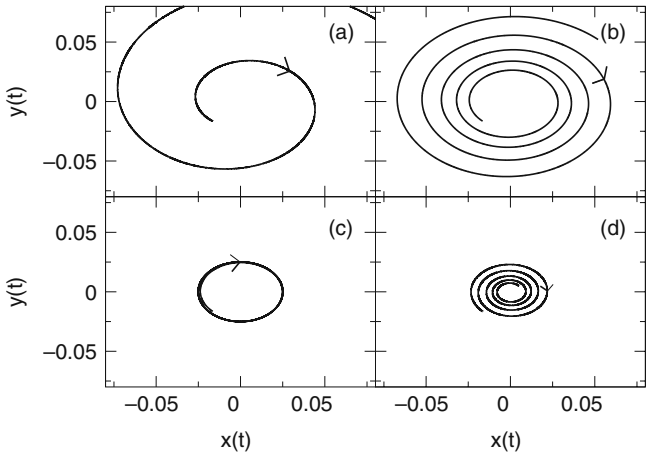

Fig. 4.2 Control of an unstable focus with $\lambda = 0.5$ and $\omega = \pi$ in the configuration space for different values of the feedback gain K. Panels (**a**), (**b**), (**c**), and (**d**) correspond to $K = 0, 0.2, 0.25$, and 0.3, respectively. The time delay τ of the TDAS control scheme is chosen as 1 corresponding to $\tau = T_0/2 = \pi/\omega$ [48]

so that the complex eigenvalues Λ are given in the presence of a control force by the implicit equation

$$\lambda \pm i\omega = \Lambda + K\left(1 - e^{-\Lambda\tau}\right). \tag{4.8}$$

Using the Lambert function W, which is defined as the inverse function of $g(z) = ze^z$ for complex z [51, 107–111], (4.8) can be solved analytically

$$\Lambda\tau = W\left(K\tau e^{-(\lambda\pm i\omega)\tau + K\tau}\right) + (\lambda \pm i\omega)\tau - K\tau. \tag{4.9}$$

Panel (a) of Fig. 4.3 shows the dependence of the largest real part of the complex eigenvalues Λ upon the time delay τ according to (4.8) and (4.9) for $\lambda = 0.5$ and $\omega = \pi$. The solid curve corresponds to a feedback gain of $K = 0.3$, the dashed curve to $K = 0.25$, and the dotted curve to $K = 0.2$. All curves start at $\mathrm{Re}(\Lambda) = \lambda$ for $\tau = 0$, i.e., when no control is applied to system. For increasing time delay, the real part $\mathrm{Re}(\Lambda)$ decreases. It can be seen in the case of $K = 0.3$ that there exist values of the time delay for which $\mathrm{Re}(\Lambda)$ becomes negative, and thus the control is successful. The curve for $K = 0.25$ shows the threshold case where $\mathrm{Re}(\Lambda)$ becomes zero for $\tau = 1$, but does not change sign. The TDAS control scheme generates an infinite number of additional eigenmodes. The corresponding eigenvalues are the solutions of the transcendental equation (4.8). The real parts of the eigenvalues all originate from $-\infty$ for $\tau = 0$. Some of these lower eigenvalues are displayed for $K = 0.3$. The different branches of the eigenvalue spectrum originate from the multiple-leaf structure of the complex Lambert function. The real part of each eigenvalue branch exhibits a typical nonmonotonic dependence upon τ which leads to crossover of different branches resulting in an oscillatory modulation of the largest real part as a function of τ. Such behavior of the eigenvalue spectrum appears to be quite general and has been found for various delayed feedback coupling schemes, including the Floquet spectrum of unstable periodic orbits [11, 86] and applications to noise-induced motion where the fixed point is stable [26].

The notch at $\tau = 1$ corresponds to Fig. 4.2, so that at this value of τ the solid, dashed, and dotted curves correspond to panels (d), (c), and (b) of Fig. 4.2, respectively. The notches at larger τ become less pronounced leading to less effective realization of the TDAS control scheme, i.e., a smaller or no τ interval with negative $\mathrm{Re}(\Lambda)$.

In the case of an unstable periodic orbit, the optimal time delay is equal to the period of the orbit to be stabilized. Note that in the case of an unstable steady state, however, the time delay is not so obviously related to a parameter of the system. We will see later which combinations of the feedback gain K and the time delay τ lead to successful control.

Panel (b) of Fig. 4.3 displays the time evolution of $x(t)$ and its time-delayed counterpart $x(t-\tau)$ in the case of a combination of $K = 0.3$ and $\tau = 1$ that leads to successful control as in panel (d) of Fig. 4.2. The x component of the control force can be calculated from the difference of the two curves and subsequent multiplication by K. Since $x(t)$ tends to zero in the limit of large t (the system reaches the focus

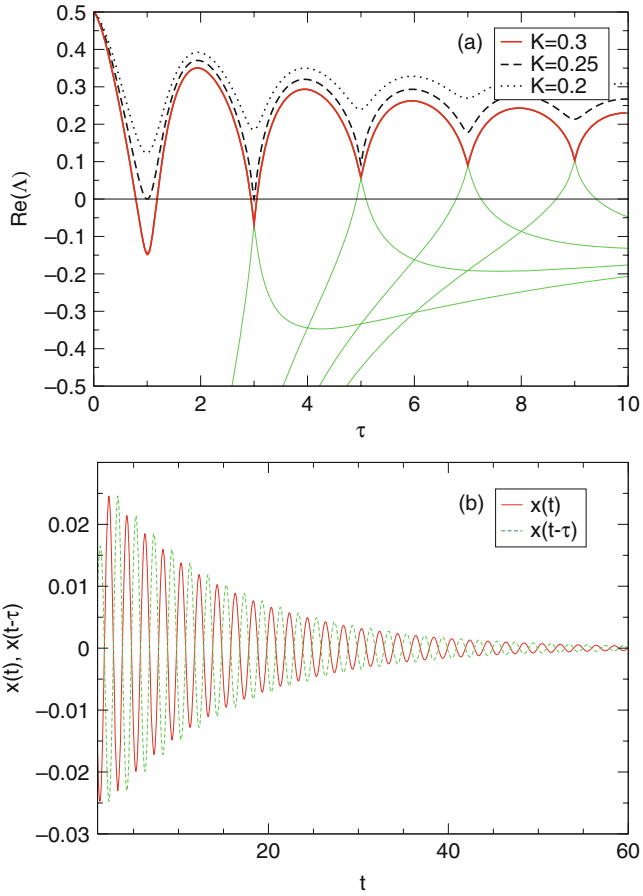

Fig. 4.3 (**a**) Largest real part of the complex eigenvalues Λ vs. τ for $\lambda = 0.5$ and $\omega = \pi$ for different K. Some lower eigenvalues are also displayed for $K = 0.3$ (*green*). (**b**) Time series of the x component of the unstable focus: the solid line (*red*) corresponds to $x(t)$ and the dashed line (*green*) to the delayed x component $x(t - \tau)$ with $\tau = 1$. The parameters of the unstable focus and the control scheme are as in panel (**d**) of Fig. 4.2 [48]

located at the origin), the control force vanishes if the system is stabilized. Thus the control scheme is non-invasive. Note that the current signal (red) and its delayed counterpart (green) are in antiphase.

In the following discussion, it is helpful to consider the real and imaginary part of (4.8) separately in order to gain some analytic information about the domain of control:

$$\begin{aligned} p + K\left[1 - e^{-p\tau}\cos(q\tau)\right] &= \lambda \\ q + Ke^{-p\tau}\sin(q\tau) &= \omega \end{aligned} \tag{4.10}$$

with $\Lambda = p + iq$.

The calculation can be done analytically for special points by using, for instance, that $p = 0$ at the threshold of control. Furthermore, we will present an expansion around the minimum value of K that reveals further details of the shape of the domain of control.

At the threshold of control the sign of the real part p of the exponent Λ changes. Therefore, setting p equal to zero in the real and imaginary parts, respectively, of (4.10) yields

$$\lambda = K\left[1 - \cos(q\tau)\right] \tag{4.11}$$

and

$$\omega = q + K\sin(q\tau). \tag{4.12}$$

Since the cosine is bounded between -1 and 1, the following inequality follows from (4.11):

$$\frac{\lambda}{2} \leq K. \tag{4.13}$$

Thus a minimum value of K, $K_{\min} = \lambda/2$, for which the control starts, can be inferred. It corresponds to $q\tau = (2n+1)\pi$ for $n = 0, 1, 2, \ldots$. It should be noted that a similar characteristic equation as (4.8) holds for the Floquet exponents of a unstable periodic orbit, where the lower bound, $K_{\min} = \lambda/2$, of the feedback gain has been shown to correspond to the flip threshold of control [43, 112].

In order to express the values of the time delay τ that correspond to the minimum K in terms of the parameters of the uncontrolled system, it is useful to consider even and odd multiples of π for $q\tau$, i.e., $q\tau = 2n\pi$ and $q\tau = (2n+1)\pi$ for $n = 0, 1, 2, \ldots$. In both cases, the imaginary part of (4.8) leads to $q = \omega$. Hence, in the latter case, the time delay τ for $K_{\min} = \lambda/2$ becomes

$$\tau = \frac{\pi}{\omega}(2n+1). \tag{4.14}$$

The last expression can be rewritten using the uncontrolled eigenperiod T_0

$$\tau = T_0\frac{2n+1}{2}, \tag{4.15}$$

where T_0 is defined by

$$T_0 = \frac{2\pi}{\omega}. \tag{4.16}$$

This discussion has shown that $K = \lambda/2$ and $\tau = T_0(2n+1)/2$ with $n = 0, 1, 2, \ldots$ correspond to points of successful control in the (K, τ) plane with minimum feedback gain.

For even multiples, i.e., $q\tau = 2n\pi$ for $n = 0, 1, 2, \ldots$, no control is possible for finite values of K, since

$$\frac{K-\lambda}{K} = \cos(q\tau)|_{q\tau=2n\pi} \tag{4.17}$$

$$\Leftrightarrow 1 - \frac{\lambda}{K} = 1, \tag{4.18}$$

which cannot be satisfied for $\lambda \neq 0$ and finite K. Furthermore, (4.12) yields that for time delays which are integer multiples of the eigenperiod, i.e., $\tau = T_0 n = 2\pi n/\omega$ with $n = 0, 1, 2, \ldots$, the control scheme fails for any feedback gain.

Another result that can be derived from (4.8) is a shift of q for increasing K. For this, taking the square of the real and imaginary part of (4.8) and using trigonometrical identities yields

$$q = \omega \mp \sqrt{(2K-\lambda)\lambda}. \tag{4.19}$$

Inserting (4.19) into the real part of (4.8) leads to an explicit expression for the dependence of time delay τ on the feedback gain K at the threshold of stability, i.e., the boundary of the control domain $p = 0$,

$$\frac{K-\lambda}{K} = \cos(q\tau) \tag{4.20}$$

$$\Leftrightarrow \quad \tau(K) = \frac{\arccos\left(\frac{K-\lambda}{K}\right)}{\omega \mp \sqrt{(2K-\lambda)\lambda}}. \tag{4.21}$$

In order to visualize the shape of the domain of control we will investigate how small deviations $\epsilon > 0$ from $K_{\min}$, i.e, $K = \lambda/2 + \epsilon$, influence the corresponding values of the time delay τ. For this, let $\eta > 0$ be small and $\tau = \frac{\pi}{\omega}(2n+1) \pm \eta$ a small deviation from τ at $K_{\min}$. Inserting the expression for K and τ into (4.20) yields after some Taylor's expansions:

$$-1 + \frac{4}{\lambda}\epsilon = -1 + \frac{1}{2}\left[\omega\eta \mp \frac{\pi}{\omega}(2n+1)\sqrt{2\lambda}\sqrt{\epsilon}\right]^2 \tag{4.22}$$

$$\Leftrightarrow \quad \eta = \left[\pm\frac{2\sqrt{2}}{\omega\sqrt{\lambda}} + \frac{\sqrt{2}\pi}{\omega^2}(2n+1)\sqrt{\lambda}\right]\sqrt{\epsilon}. \tag{4.23}$$

This equation describes the shape of the domain of control at the threshold of stabilization, i.e., $p = 0$, near the minimum K value at $\tau = T_0(2n+1)/2$ in the (K, τ) control plane. Small deviations from τ at $K_{\min}$ are influenced by the square root of small deviations from the minimum feedback gain.

Figure 4.4 displays the largest real part of the eigenvalues Λ in dependence on both the feedback gain K and the time delay τ for $\omega = \pi$ and two different values of λ and summarizes the results of this section. The values of Λ are calculated using

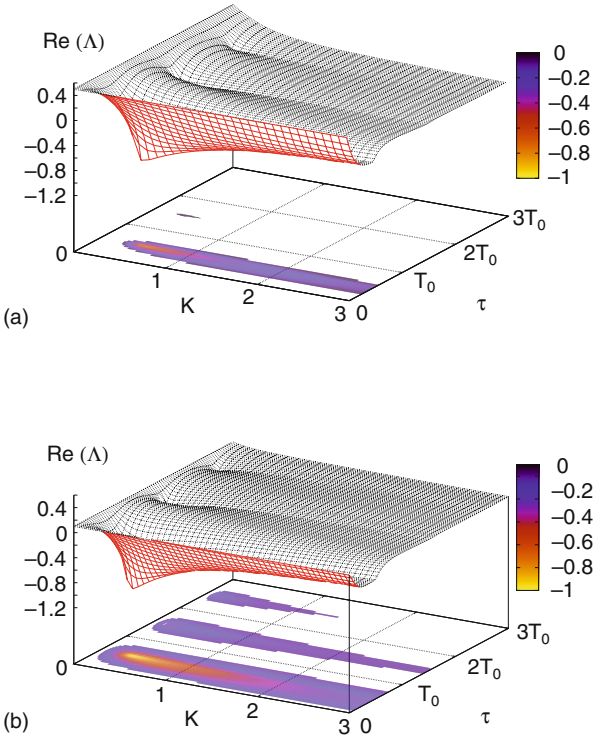

Fig. 4.4 Domain of control in the (K, τ) plane and largest real part of the complex eigenvalues Λ as a function of K and τ according to (4.9). The two-dimensional projection at the *bottom* shows combinations of τ and K, for which $\mathrm{Re}(\Lambda)$ is negative and thus the control successful [panel (**a**): $\lambda = 0.5$ and $\omega = \pi$; panel (**b**): $\lambda = 0.1$ and $\omega = \pi$] [48]

the analytic solution (4.9) of (4.8). The two-dimensional projections at the bottom of each plot extract combinations of K and τ with negative p, i.e., successful control of the system. In the absence of a control force, i.e., $K = 0$, the real part of Λ starts at λ. Increasing the feedback gain decreases $\mathrm{Re}(\Lambda)$. For $K = K_{\min} = \lambda/2$, the real part of the eigenvalue reaches 0 for certain time delays, i.e., $\tau = T_0(2n+1)/2$ with $n = 0, 1, 2, \ldots$, and then changes sign. Thus, the system is stabilized. For values of the feedback gain slightly above the minimum value $K_{\min}$, the domain of control shows a square root shape. It can be seen that for time delays of $\tau = T_0 n$, the largest real part of the eigenvalues remains positive for any feedback gain. For a smaller value of λ (Fig. 4.4b), i.e., closer to the instability threshold of the fixed point, the domains of control become larger.

An example of the combination of minimum feedback gain $K_{\min} = \lambda/2$ and corresponding time delay $\tau = T_0(2n+1)/2$, $n = 0, 1, 2, \ldots$ is shown in panel (c) of Fig. 4.2, where $K = \lambda/2 = 0.25$ and $\tau = T_0/2 = \pi/\omega = 1$. It describes the control threshold case between stable and unstable fixed point.

Socolar et al. introduced an extension of the Pyragas method by taking states into account which are delayed by integer multiples of τ [39]. This method is known as *extended time-delay autosynchronization* or ETDAS. Calculating the difference between two states which are one time unit τ apart yields the following control force, which can be written in three equivalent forms:

$$\mathbf{F}(t) = K \sum_{n=0}^{\infty} R^n \left[\mathbf{x}(t - n\tau) - \mathbf{x}(t - (n+1)\tau)\right] \tag{4.24}$$

$$= K \left[\mathbf{x}(t) - (1-R) \sum_{n=1}^{\infty} R^{n-1} \mathbf{x}(t - n\tau)\right] \tag{4.25}$$

$$= K \left[\mathbf{x}(t) - \mathbf{x}(t-\tau)\right] + R\mathbf{F}(t-\tau), \tag{4.26}$$

where K and τ denote the (real) feedback gain and the time delay, respectively. $R \in (-1, 1)$ is a memory parameter that takes into account those states that are delayed by more than one time interval τ. Note that $R = 0$ yields the TDAS control scheme introduced by Pyragas [6].

The first form of the control force, (4.24), indicates the non-invasiveness of the ETDAS method because $\mathbf{x}^*(t-\tau) = \mathbf{x}^*(t)$ if the fixed point is stabilized. The third form, (4.26), is suited best for an experimental implementation since it involves states further than τ in the past only recursively.

While the stability of the fixed point in the absence of control is given by the eigenvalues of matrix $\mathbf{A}$, i.e., $\lambda \pm i\omega$, one has to solve the following characteristic equation in the case of an ETDAS control force [50]:

$$\Lambda + K \frac{1 - e^{-\Lambda\tau}}{1 - Re^{-\Lambda\tau}} = \lambda \pm i\omega. \tag{4.27}$$

Due to the presence of the time delay τ, this characteristic equation becomes transcendental and possesses an infinite but countable set of complex solutions Λ. For nonzero memory parameter R, (4.27) must be solved numerically.

Figure 4.5 depicts the dependence of the largest real parts of the eigenvalue Λ upon the time delay τ according to (4.27) for different memory parameters R and fixed feedback gain $K = 0.3$. The dashed, dotted, solid, dash-dotted, and dash-double-dotted curves (red, green, black, blue, and magenta) of $\mathrm{Re}(\Lambda)$ correspond to $R = -0.7, -0.35, 0, 0.35$, and 0.7, respectively. The parameters of the unstable focus are chosen as $\lambda = 0.1$ and $\omega = \pi$. Note that the time delay τ is given in units of the intrinsic period $T_0 = 2\pi/\omega$. When no control is applied to the system, i.e., $\tau = 0$, all curves start at λ which corresponds to the real part of the uncontrolled eigenvalue. For increasing time delay, the real part of Λ decreases and eventually changes sign. Thus, the fixed point becomes stable. Note that there is a minimum of $\mathrm{Re}(\Lambda)$ indicating strongest stability if the time delay τ is equal to half the intrinsic period. For larger values of τ, the real part increases and becomes positive again. Hence, the system loses its stability. Above $\tau = T_0$, the cycle is repeated but the

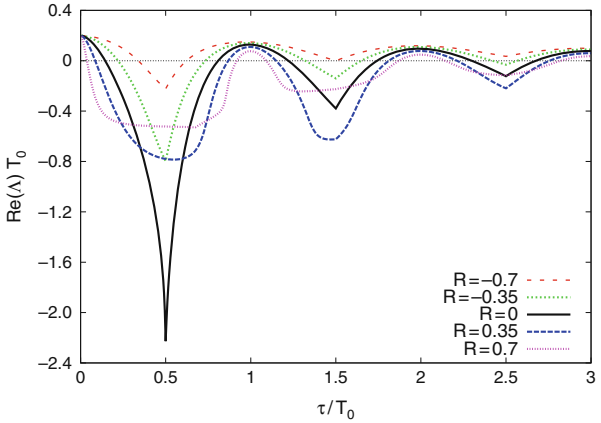

Fig. 4.5 Largest real part of the complex eigenvalues Λ as a function of τ for different values of R. The *dashed*, *dotted*, *solid*, *dash-dotted*, and *dash-double-dotted* curves (*red*, *green*, *black*, *blue*, and *magenta*) correspond to $R = -0.7, -0.35, 0, 0.35$, and 0.7, respectively. The parameters of the unstable focus are chosen as $\lambda = 0.1$ and $\omega = \pi$ which yields an intrinsic period $T_0 = 2\pi/\omega = 2$. The feedback gain K is fixed at $KT_0 = 0.6$ [50]

minimum of $\mathrm{Re}(\Lambda)$ is not so deep. The control method is less effective because the system has already evolved further away from the fixed point. For vanishing memory parameter $R = 0$ (TDAS), the minimum is deepest, however, the control interval, i.e., values of τ with negative real parts of Λ, increases for larger R. Therefore the ETDAS control method is superior in comparison to the Pyragas scheme.

Figure 4.6 shows the domain of control in the plane parametrized by the feedback gain K and time delay τ for different values of R:0, 0.35, 0.7, and -0.35 in panels

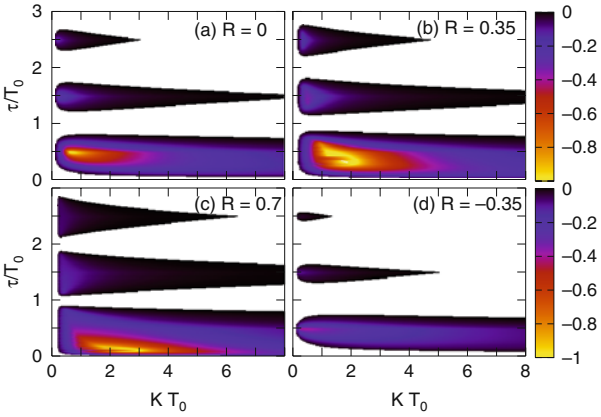

Fig. 4.6 Domain of control in the (K, τ) plane for different values of R:0, 0.35, 0.7, and -0.35 in panels (**a**), (**b**), (**c**), and (**d**), respectively. The grayscale (*color code*) shows only negative values of the largest real part of the complex eigenvalues Λ according to (4.27). The parameters of the system are as in Fig. 4.5 [50]

(a), (b), (c), and (d), respectively. The grayscale (color code) indicates only negative values of the largest real parts of the complex eigenvalue Λ. Therefore, Fig. 4.5 can be understood as a vertical cut through Fig. 4.6 for a fixed value of $KT_0 = 0.6$. Each panel displays several islands of stability which shrink for larger time delays τ. Note that no stabilization is possible if τ is equal to an integer multiple of the intrinsic period T_0. The domains of control become larger if the memory parameter R is closer to 1.

In order to obtain some analytic information of the domain of control, it is helpful to separate the characteristic equation (4.27) into real and imaginary parts. This yields using $\Lambda = p + iq$:

$$K(1 - e^{-p\tau}\cos q\tau) = \lambda - p - Re^{-p\tau}[(\lambda - p)\cos q\tau \pm (\omega - q)\sin q\tau] \quad (4.28)$$

and

$$Ke^{-p\tau}\sin q\tau = \pm(\omega - q) + Re^{-p\tau}[(\lambda - p)\sin q\tau \pm (\omega - q)\cos q\tau]. \quad (4.29)$$

The boundary of the domain of controls is determined by a vanishing real part of Λ, i.e., $p = 0$. With this constraint, (4.28) and (4.29) can be rewritten as

$$\begin{aligned} K(1 - \cos q\tau) &= \lambda - R[\lambda\cos q\tau \pm (\omega - q)\sin q\tau], \\ K\sin q\tau &= \pm(\omega - q) + R[\lambda\sin q\tau \pm (\omega - q)\cos q\tau]. \end{aligned} \quad (4.30)$$

At the threshold of control ($p = 0$, $q = \omega$), there is a certain value of the time delay, which will serve as a reference in the following, given by

$$\tau = \frac{(2n+1)\,\pi}{\omega} = \left(n + \frac{1}{2}\right) T_0, \quad (4.31)$$

where n is any nonnegative integer. For this special choice of the time delay, the range of possible feedback gains K in the domain of control becomes largest as can be seen in Fig. 4.6. Hence, we will refer to this τ value as optimal time delay in the following. The minimum feedback gain at this τ can be obtained:

$$K_{\min}(R) = \frac{\lambda\,(1+R)}{2}. \quad (4.32)$$

Extracting an expression for $\sin(q\tau)$ from (4.30) and inserting it into the equation for the imaginary part leads after some algebraic manipulation to a general dependence of K on the imaginary part q of Λ:

$$K(q) = \frac{(1+R)\left[\lambda^2 + (\omega - q)^2\right]}{2\lambda}. \quad (4.33)$$

Taking into account the multivalued properties of the arcsine function, this yields in turn analytical expressions of the time delay in dependence on q:

$$\tau_1(q) = \frac{\arcsin\left(\dfrac{2\lambda(1-R^2)(\omega-q)}{\lambda^2(1-R^2)^2+(\omega-q)^2(1+R)^2}\right)+2n\pi}{q}, \qquad (4.34)$$

$$\tau_2(q) = \frac{-\arcsin\left(\dfrac{2\lambda(1-R^2)(\omega-q)}{\lambda^2(1-R^2)^2+(\omega-q)^2(1+R)^2}\right)+(2n+1)\pi}{q},$$

where n is a nonnegative integer. Together with (4.33), these formulas describe the boundary of the domain of control in Fig. 4.6. Note that two expressions τ_1 and τ_2 are necessary to capture the complete boundary.

For a better understanding of effects due to the memory parameter R, it is instructive to consider the domain of control in the plane parametrized by R and the feedback gain K. The results can be seen in Fig. 4.7, where the black, medium gray, dark gray, and light gray areas (blue, green, red, and yellow) correspond to the domain of control for $\lambda T_0 = 0.2, 1, 5$, and 10, respectively. The other system parameter is chosen as $\omega = \pi$. We keep the time delay constant at $\tau = T_0/2$. Note that the K interval for successful control increases for larger values of R. In fact, while the original Pyragas scheme, i.e., $R = 0$, fails for $\lambda T_0 = 10$, the ETDAS method is still able to stabilize the fixed point. The upper left boundary corresponds to (4.32). The lower right boundary can be described by a parametric representation which can be derived from the characteristic equation (4.27):

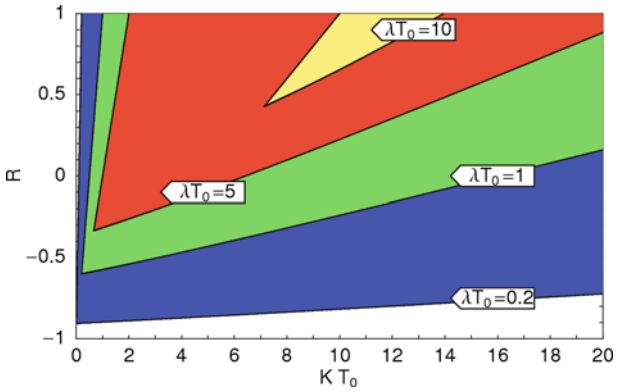

Fig. 4.7 Domain of control in the (K, R) plane for different values of λ. The *black*, *medium gray*, *dark gray*, and *light gray* domains (*blue, green, red*, and *yellow*) correspond to $\lambda T_0 = 0.2, 1, 5$, and 10, respectively, as indicated. The time delay is chosen as $\tau = T_0/2$ and $\omega = \pi$ [50]

$$R = \frac{\lambda\tau - \vartheta \tan(\vartheta/2)}{\lambda\tau + \vartheta \tan(\vartheta/2)}, \tag{4.35}$$

$$K\tau = \frac{\vartheta^2 + (\lambda\tau)^2}{\lambda\tau + \vartheta \tan(\vartheta/2)}, \tag{4.36}$$

where we used the abbreviation $\vartheta = (q - \omega)\,\tau$ for notational convenience. The range of ϑ is given by $\vartheta \in [0, \pi)$. A linear approximation leads to an analytic dependence of R and the feedback gain K given by a function $R(K)$ instead of the parametric equations (4.35) and (4.36). A Taylor expansion around $\vartheta = \pi$ yields

$$K_{\max}(R) = \frac{\lambda^2 + \pi^2}{2\lambda}\,(R + 1) + 2\,(R - 1)\,. \tag{4.37}$$

Another representation of the superior control ability of ETDAS is depicted in Fig. 4.8. The domain of control is given in the (K, λ) plan for different values of R. The light gray, dark gray, medium gray, and black areas (yellow, red, green, and blue) refer to $R = -0.35$, 0 (TDAS), 0.35, and 0.7, respectively. The time delay is chosen as $\tau = T_0/2$. One can see that for increasing R, the ETDAS method can stabilize systems in a larger λ range. However, the corresponding K interval for successful control can become small. See, for instance, the black (blue) area ($R = 0.7$) for large λ. A similar behavior was found in the case of stabilization of an unstable periodic orbit by ETDAS [112]. We stress that, as in the case of periodic orbits, the boundaries of the shaded areas can be calculated analytically from the following expression:

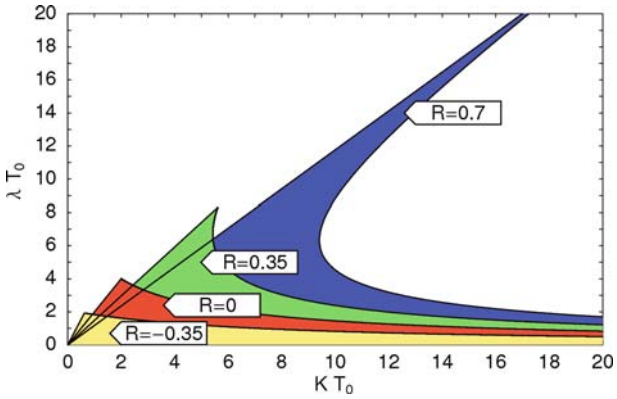

Fig. 4.8 Domain of control in the (K, λ) plane for different memory parameters R. The *light gray*, *dark gray*, *medium gray*, and *black domains* (*yellow*, *red*, *green*, and *blue*) areas correspond to $R = -0.35$, 0 (TDAS), 0.35, and 0.7, respectively. The time delay is fixed at $\tau = T_0/2$ [50]

$$K\tau = \frac{(1-R)\vartheta}{\tan(\vartheta/2)}\left[\left(\frac{1+R}{1-R}\right)^2 + \tan^2(\vartheta/2)\right], \tag{4.38}$$

$$\lambda\tau = \frac{\vartheta}{\tan(\vartheta/2)}\left(\frac{1+R}{1-R}\right), \tag{4.39}$$

where we used $\vartheta = (q-\omega)\,\tau$ with $\vartheta \in [0,\pi)$ as in (4.35) and (4.36). The maximum value for λ, which can be stabilized, is given by the special case $\vartheta = 0$:

$$\lambda_{\max}\tau = 2\,\frac{1+R}{1-R}. \tag{4.40}$$

Extensions to include latency effects associated with the generation and injection of the feedback signal, low-pass and bandpass filtering in the control loop, and non-diagonal control schemes incorporating a feedback phase, have been discussed elsewhere [48, 50].

4.2.2 Asymptotic Properties

It is the purpose of this section to obtain deeper analytical insight into the time-delayed feedback control of steady states for large delay by relating asymptotic properties of the eigenvalue spectrum with the exact solutions and by discussing the shape of the control domain in the space of the control parameters [49].

Three different timescales are of importance in such a control problem: (i) the inverse divergence rate of trajectories around the unstable fixed point $1/\lambda$, (ii) the period of undamped oscillations around the fixed point $T_0 = 2\pi/\omega$, where ω is the oscillation frequency, and (iii) the delay time τ used in the feedback control loop. Here we consider the case $\tau \gg 1/\lambda$ and study again a generic model equation which describes an unstable focus above a Hopf bifurcation and is given by (4.6).

Note that, due to the presence of the delay, (4.8) possesses infinitely many solutions. Nevertheless, the stability of the fixed point is determined by a finite number of critical roots with largest real parts [110]. As a result, the stabilization problem consists in determining these critical eigenvalues and describing their behavior. In particular, successful control is achieved by providing conditions in terms of the control parameters K and τ for which all critical eigenvalues have negative real parts.

Figure 4.9 shows the real parts of the critical eigenvalues Λ as a function of τ for different values of K. The insets show the same eigenvalues as curves in the complex plane parametrized by τ. Note that the eigenvalue originating from the uncontrolled system (red) is the most unstable one for sufficiently small K and does not couple to the eigenvalues generated by the delay (see Fig. 4.9 a,b). The countable set of eigenvalues generated by the delay originates from $\mathrm{Re}\,\Lambda = -\infty$ for $\tau \to 0$ and shows the typical nonmonotonic behavior that leads to stability islands for appropriate τ and K [48]. For larger values of K, the eigenvalue originating from

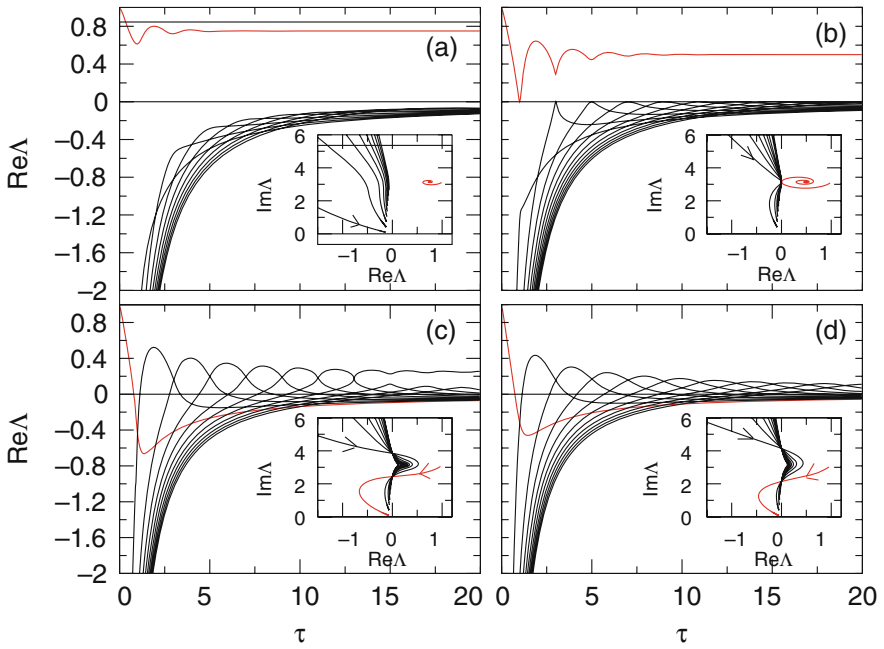

Fig. 4.9 Real parts of the complex eigenvalues Λ as a function of τ calculated from the characteristic equation (4.8) for 10 modes with the largest real parts. (**a**) $K = 0.25$, (**b**) $K = 0.5$, (**c**) $K = 0.75$, and (**d**) $K = 1.0$. Inset: eigenmodes Λ in the complex plane for $\tau \in [0, 20]$. *Red curves*: eigenvalue originating from the uncontrolled system; *black curves*: eigenmodes created by the delay control. Parameters: $\omega = \pi$ and $\lambda = 1$ [49]

the uncontrolled system is no longer separated from those which are generated by the delay (see Fig. 4.9 c,d). Moreover, one can observe a scaling behavior of the real parts of the eigenvalues for large τ in Fig. 4.9(a-c), there is a single eigenvalue retaining a positive real part, whereas all the other real parts tend to zero for large τ. The insets show that the eigenvalues in fact accumulate along the imaginary axis. This observation will be studied in detail in the following.

The scaling behavior of eigenvalues of general linear delay-differential equations for large delay τ has been analyzed in [113]. In particular, it turns out that one can distinguish the following.

(a) *Strongly unstable eigenvalues* Λ_s which have positive real parts that do not tend to zero with increasing τ, i.e., $\Lambda_s \to$ const and $\mathrm{Re}\,\Lambda_s \geq \delta$ for some $\delta > 0$ as $\tau \to \infty$.

(b) *Pseudocontinuous spectrum* of eigenvalues Λ_p with real parts that scale as $1/\tau$, i.e., $\Lambda_p = \frac{1}{\tau}\gamma + i\left(\Omega + \frac{1}{\tau}\varphi\right) + \mathcal{O}\left(\frac{1}{\tau^2}\right)$ with some γ, Ω, and φ. A spectrum with this scaling behavior and positive real part leads to so-called *weak instabilities* (for more details, see [114, 113]).

In order to obtain the strongly unstable eigenvalues, we insert $\Lambda_s = \text{const}$ into (4.8) and assume $\tau \to \infty$. Since $\text{Re}\Lambda_s > \delta$, the exponential term vanishes and we arrive at the expression for Λ_s:

$$\Lambda_s = \lambda - K \pm i\omega,$$

which holds for $\lambda - K > 0$. Thus we obtain the following statement:

(i) For $K < \lambda$, there exist two eigenvalues of the controlled stationary state, Λ_{s1} and its complex conjugate Λ_{s2}, such that $\Lambda_{s1} \to \lambda - K + i\omega$ as $\tau \to \infty$. The real parts of these eigenvalues are positive and, hence, the stationary state is *strongly unstable* (cf. Fig. 4.9(a-c)).

In order to obtain the asymptotic expression for the remaining pseudo-continuous part of the spectrum, we have to insert the scaling $\Lambda_p = \frac{1}{\tau}\gamma + i\left(\Omega + \frac{1}{\tau}\varphi\right)$ into (4.8). Up to the leading order we obtain the equation

$$i\Omega + K\left(1 - e^{-\gamma}e^{-i\varphi}\right) = \lambda \pm i\omega, \tag{4.41}$$

and the additional condition $\Omega = \Omega^{(m)} = 2\pi m/\tau$, $m = \pm 1, \pm 2, \pm 3, ...$, (4.41) can be solved with respect to $\gamma(\Omega)$:

$$\gamma(\Omega) = -\frac{1}{2}\ln\left[\left(1 - \frac{\lambda}{K}\right)^2 + \left(\frac{\Omega \pm \omega}{K}\right)^2\right]. \tag{4.42}$$

The fact that $\text{Re}\,\Lambda_p \approx \gamma(\Omega)/\tau$ and $\text{Im}\,\Lambda_p \approx \Omega$ up to the leading order means that the eigenvalues Λ_p accumulate in the complex plane along curves $(\gamma(\Omega), \Omega)$, provided that the real axis is scaled as $\tau\text{Re}\,\Lambda$. The actual positions of the eigenvalues on the curves can be obtained by evaluating Ω at points $\Omega^{(m)} = 2\pi m/\tau$. With increasing τ, the eigenvalues cover the curves densely [113]. Hence, we obtain the second statement:

(ii) The fixed point of system (4.6) has a set of eigenvalues which behave asymptotically as $\Lambda_p(\Omega^{(k)}) = \frac{1}{\tau}\gamma(\Omega^{(k)}) + i\left(\Omega^{(k)} + \frac{1}{\tau}\varphi(\Omega^{(k)})\right)$ with $\gamma(\Omega)$ given by (4.42). We have *weak instability* if the maximum of $\gamma(\Omega)$ is positive, i.e.,

$$\gamma_{\max} = \max_{\Omega}\gamma(\Omega) = -\ln\left|1 - \frac{\lambda}{K}\right| > 0,$$

which is the case for $K > \lambda/2$.

Figure 4.10 illustrates the spectrum of the fixed point of system (4.6) for $\tau = 20$. One can clearly distinguish the two types of eigenvalues. For $K < \lambda/2$ (Fig. 4.10a), the fixed point has a pair of strongly unstable eigenvalues, whereas the pseudocontinuous spectrum is stable. Note that the symbols (red) show the spectrum computed numerically from the full eigenvalue equation, whereas the dashed lines are the curves $(\gamma(\Omega), \Omega)$ from the asymptotic approximation where the pseudocontinuous

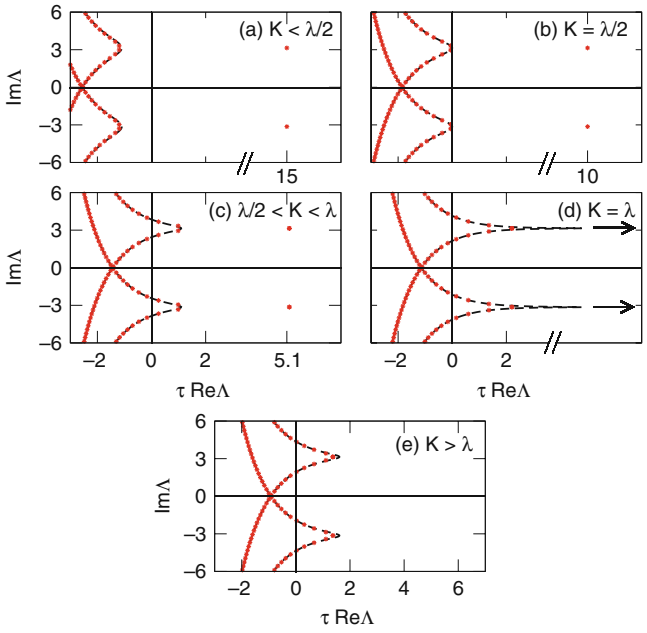

Fig. 4.10 Numerically computed spectrum of eigenvalues for $\tau = 20$ (*asterisks, red*). The *dashed lines* depict the asymptotic pseudocontinuous spectrum. (**a**) Strong instability for $K = 0.25$ ($K < \lambda/2$); (**b**) $K = 0.5 = \lambda/2$, critical case at which the weak instability occurs in addition to the strong one; (**c**) $K = 0.75$ ($\lambda/2 < K < \lambda$), strong and weak instability; (**d**) $K = 1.0 = \lambda$, critical case at which a strong instability disappears via the singularity of the pseudocontinuous spectrum; and (**e**) $K = 1.25$ ($K > \lambda$), weak instability. Parameters: $\omega = \pi$ and $\lambda = 1$ [49]

spectrum accumulates for large τ. At $K = \lambda/2$ (cf. Fig. 4.10b), the pseudocontinuous spectrum touches the imaginary axis resulting in the appearance of a weak instability for $K > \lambda/2$. This leads to the coexistence of strong and weak instabilities for $\lambda/2 < K < \lambda$ (Fig. 4.10c). At $K = \lambda$, the strongly unstable eigenvalues disappear, being absorbed by the pseudocontinuous spectrum, which develops a singularity at this moment, cf. Fig. 4.10(d). Finally, for $K > \lambda$ (Fig. 4.10e), there occurs only a weak instability induced by the pseudocontinuous spectrum.

After inspecting all possibilities given in Fig. 4.10, we conclude that stabilization by the feedback control scheme (4.6) always has an upper limit τ_c such that for $\tau > \tau_c$ it fails. Additionally, we note that for $K < \lambda$ and large delay, the stationary state is strongly unstable with the complex conjugate eigenvalues $\Lambda_{1,2} = \lambda - K \pm i\omega$, and for $K > \lambda$ weakly unstable with a large number of unstable eigenvalues given by (4.41), the real parts of which scale as $1/\tau$.

Next, we show that strongly delayed feedback can stabilize a fixed point in the case when the fixed point is sufficiently close to the Hopf bifurcation. In our case this means that λ is small. In particular, we are going to prove that the delayed feedback control scheme will be successful even for large delay within the range of order $1/\lambda^2$. We will also provide conditions for successful control.

For the fixed point, which is close to the Hopf bifurcation, we assume $K > \lambda$, and hence it has an unstable pseudocontinuous spectrum as shown in Fig. 4.10(e). As λ stays fixed, with increasing τ the curve of the pseudocontinuous spectrum will be densely filled with the eigenvalues ($\Omega^{(m)} = 2\pi m/\tau$). The only possibility for the fixed point to become stable is to assume that λ is also scaled with increasing τ. Particularly, we will show that in order to achieve control we have to scale it as $\lambda = \lambda_0 \varepsilon^2$ with fixed λ_0 (here for convenience we introduce the small parameter $\varepsilon = 1/\tau$).

Figure 4.11 illustrates the part of the curve $\gamma(\Omega)$ which may induce an instability in the system. More precisely, the interval of unstable frequencies is $\Omega_1 < \Omega < \Omega_2$, where Ω_1 and Ω_2 are given by the zeros of $\gamma(\Omega)$:

$$\Omega_{1,2} = \omega \pm K\sqrt{1 - \left(1 - \frac{\lambda}{K}\right)^2}.$$

For small λ we can approximate this as

$$\Omega_{1,2} = \omega \pm \sqrt{2\lambda K}. \tag{4.43}$$

The length of the interval of unstable frequencies is $\Delta\Omega = \Omega_2 - \Omega_1 = 2\sqrt{2\lambda K}$.

We note that the actual position of the eigenvalues on the curve corresponds to the values of $\Omega^{(m)} = 2\pi m\varepsilon$ with any integer m. It is easy to see that the distance between the frequencies of neighboring eigenvalues $\Omega^{(m+1)} - \Omega^{(m)} = 2\pi\varepsilon$ scales as ε. Therefore, the control can be successful if $\lambda = \lambda_0\varepsilon^2$. In this case the length of the unstable interval is $\Delta\Omega = 2\varepsilon\sqrt{2\lambda_0 K}$ and scales also as ε. The control can be achieved if the length is smaller than the distance between neighboring eigenvalues,

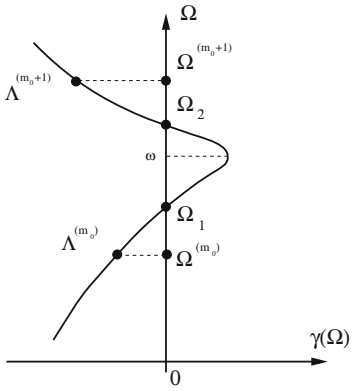

Fig. 4.11 Curve of the pseudocontinuous spectrum. The actual position of the complex eigenvalues $\Lambda = \frac{1}{\tau}\gamma + i\left(\Omega + \mathcal{O}(\frac{1}{\tau})\right)$ on the curve corresponds to $\Omega^{(m)} = 2\pi m\varepsilon$, $m = \pm 1, \pm 2, \pm 3, ...$, and $\varepsilon = 1/\tau$. The fixed point is stable if the imaginary parts of the eigenvalues are outside of the interval $\Omega_1 < \Omega < \Omega_2$. Such a case with $\Omega^{(m_0)} < \Omega_1 < \Omega_2 < \Omega^{(m_0+1)}$ is illustrated, in which the leading eigenvalues $\Lambda^{(m_0)}$ and $\Lambda^{(m_0+1)}$ have negative real parts [49]

i.e., $\Delta\Omega = 2\varepsilon\sqrt{2\lambda_0 K} < 2\pi\varepsilon$, leading to

$$K < \frac{\pi^2}{2\lambda_0}. \tag{4.44}$$

Equation (4.44) gives a necessary condition for successful control.

The relative phase of the delay plays an additional important role. Depending on this phase, control occurs periodically with τ. In order to quantify this effect, let us introduce $\omega_\tau = 2\pi/\tau$ to be the frequency associated with the delay. Then the ratio of the internal frequency ω and ω_τ is given by $\omega/\omega_\tau = \gamma_\tau \bmod 1$. Here $0 < \gamma_\tau < 1$ measures the detuning from the resonance between the internal frequency and the delay-induced one. Using this notation and (4.43), we can rewrite

$$\Omega_{1,2} = m_0\omega_\tau + \gamma_\tau\omega_\tau \pm \varepsilon\sqrt{2\lambda_0 K} = \Omega^{(m_0)} + \varepsilon\left(2\pi\gamma_\tau \pm \sqrt{2\lambda_0 K}\right).$$

Here m_0 is some integer number. The necessary and sufficient condition for the stability is (cf. Fig. 4.11) $\Omega^{(m_0)} < \Omega_1 < \Omega_2 < \Omega^{(m_0+1)}$, which leads to

$$\sqrt{2\lambda_0 K} < 2\pi \min\{\gamma_\tau, 1-\gamma_\tau\}$$

or

$$K < \frac{2\pi^2}{\lambda_0}(\min\{\gamma_\tau, 1-\gamma_\tau\})^2 = \frac{2\pi^2}{\lambda_0}\left(\min\left\{\left[\frac{\omega\tau}{2\pi}\right]_f, 1-\left[\frac{\omega\tau}{2\pi}\right]_f\right\}\right)^2, \tag{4.45}$$

where $\left[\frac{\omega\tau}{2\pi}\right]_f$ is the fractional part of $\frac{\omega\tau}{2\pi}$. Practically, one has also to satisfy $K > \lambda$, but our scaling assumes the smallness of λ. Figure 4.12 shows the domain of control given by (4.45) for $\lambda = \lambda_0/\tau^2$.

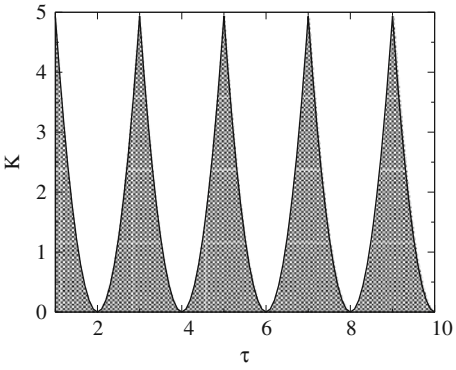

Fig. 4.12 *Shaded region*: domain of control in the (τ, K) plane for the fixed point close to the Hopf bifurcation, given by the asymptotic formula (4.45) for $\lambda = \lambda_0/\tau^2$. Parameters: $\omega = \pi$ and $\lambda_0 = 1$ [49]

In order to return to unscaled parameters, we have to substitute $\lambda_0 = \lambda/\varepsilon^2 = \lambda\tau^2$. Figure 4.13(a) shows the obtained domain of control for fixed small $\lambda = 0.01$. The maximum allowed values of K decrease as $1/\tau^2$. More precisely, we have

$$K_{\max}(\tau) = \frac{\pi^2}{2\lambda\tau^2}. \tag{4.46}$$

The application of the asymptotic analysis allows to reveal many essential features and mechanisms of the stabilization control scheme (4.6) for large delay τ. On the other hand, the obtained approximations are valid as soon as K is much larger than λ. Figure 4.13 shows a comparison of the boundaries of the control domain, which are given by the asymptotic methods and exact analytical formulas derived in the previous section. Very close to the Hopf bifurcation ($\lambda = 0.01$) the agreement is excellent even at small values of τ (Fig. 4.13a), while for larger λ (Fig. 4.13b) the deviations become more visible. In addition, the approximate solution does not give the lower boundary of the control domain for small K which only shows up in Fig. 4.14. The analytical approach also allows us to identify the "peaks" of the control domains, which occur at $\tau_{\max} = (2n+1)\pi/\omega$, $n = 0, 1, 2, ...$, as double Hopf bifurcation points. The critical time delay, above which control fails, is given by $\tau_c = 2/\lambda$.

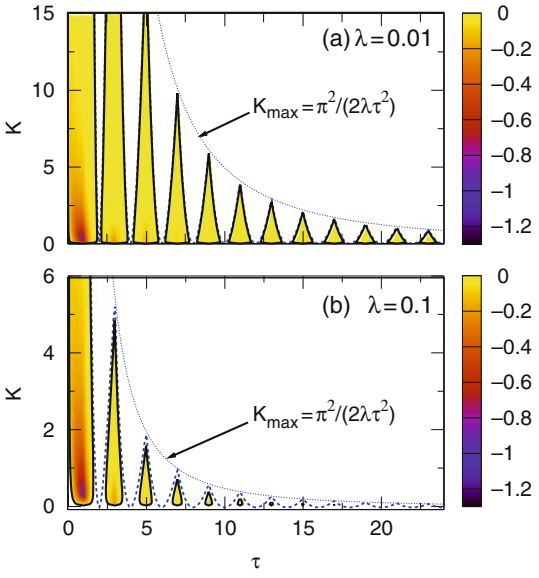

Fig. 4.13 Domain of control in the (τ, K) plane, and largest negative real part of the complex eigenvalues $\Lambda(K, \tau)$ (in *color code*) calculated from the characteristic equation using the Lambert function [(4.9)]. *Dashed lines* (*blue*): asymptotic approximation (4.45) of stability boundary; *dotted lines* (*blue*): approximate maxima (4.46); and *solid lines*: exact stability boundaries. Parameters: (**a**) $\omega = \pi$, $\lambda = 0.01$ and (**b**) $\omega = \pi$, $\lambda = 0.1$ [49]

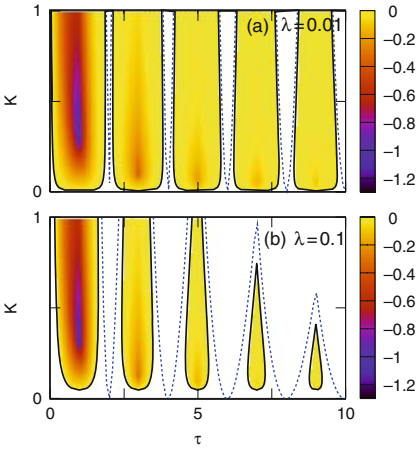

Fig. 4.14 Enlargement of Fig. 4.13: deviation of the asymptotic results (*dashed*) from the exact stability boundary (*solid*) for small K or large λ [49]

An inspection of the islands of stabilization in Figs. 4.13 and 4.14 reveals that the absolute value of the real part of the critical eigenvalue, i.e., the eigenvalue which has the largest real part (but remains negative within those islands), decreases with increasing τ. Hence, the fixed point becomes less stable, and it is expected that the system becomes more sensitive to noise and it will be more difficult to realize stabilization experimentally, if the delay time is chosen several times the system's characteristic time T_0.

4.2.3 Beyond the Odd Number Limitation of Unstable Periodic Orbits

In this section we consider the stabilization of periodic orbits by time-delayed feedback control [52]. Although time-delayed feedback control has been widely used with great success in real-world problems in physics, chemistry, biology, and medicine, e.g., [38, 64, 71–73, 115–122], severe limitations are imposed by the common belief that certain orbits cannot be stabilized for any strength of the control force. In fact, it has been contended that periodic orbits with an odd number of real Floquet multipliers greater than unity cannot be stabilized by the Pyragas method [43, 44, 123–126], even if the simple scheme is extended by multiple delays in form of an infinite series [39]. To circumvent this restriction more complicated control schemes, like an oscillating feedback [127], half-period delays for special, symmetric orbits [128], or the introduction of an additional, unstable degree of freedom [126, 129], have been proposed. Here, we show that the general limitation for orbits with an odd number of real unstable Floquet multipliers greater than unity does not hold: stabilization may be possible for suitable choices of the

feedback matrix [52, 53]. Our example consists of an unstable periodic orbit generated by a subcritical Hopf bifurcation. In particular, this refutes the theorem in [44].

Consider the normal form of a subcritical Hopf bifurcation extended by a time-delayed feedback term:

$$\dot{z}(t) = \left[\lambda + i + (1 + i\gamma)|z(t)|^2\right] z(t) + b[z(t-\tau) - z(t)], \tag{4.47}$$

with $z \in \mathbb{C}$ and real parameters λ and γ. Here the Hopf frequency is normalized to unity. The feedback matrix is represented by multiplication with a complex number $b = b_R + ib_I = b_0 e^{i\beta}$ with real b_R, b_I, β and positive b_0. Note that the nonlinearity $f(\lambda, z(t)) = \left[\lambda + i + (1 + i\gamma)|z(t)|^2\right] z(t)$ commutes with complex rotations. Therefore $\exp(i\vartheta)z(t)$ solves (4.47), for any fixed ϑ, whenever $z(t)$ does. In particular, nonresonant Hopf bifurcations from the trivial solution $z \equiv 0$ at simple imaginary eigenvalues $\eta = i\omega \neq 0$ produce rotating wave solutions $z(t) = z(0)\exp\left(i\frac{2\pi}{T}t\right)$ with period $T = 2\pi/\omega$ even in the nonlinear case and with delay terms. This follows from uniqueness of the emanating Hopf branches.

Transforming Eq. (4.47) to amplitude and phase variables r, θ using $z(t) = r(t)e^{i\theta(t)}$, we obtain at $b = 0$

$$\dot{r}(t) = \left(\lambda + r^2\right) r \tag{4.48}$$

$$\dot{\theta}(t) = 1 + \gamma r^2. \tag{4.49}$$

An unstable periodic orbit with $r = \sqrt{-\lambda}$ and period $T = 2\pi/(1 - \gamma\lambda)$ exists for $\lambda < 0$. This is the orbit we will stabilize. We will call it the Pyragas orbit. At $\lambda = 0$ a subcritical Hopf bifurcation occurs. The Pyragas control method chooses the delay time τ as $\tau_P = nT$. This eliminates the feedback term on the orbit, and thus recovers the original T-periodic solution $z(t)$. In this sense the control method is *non-invasive*.

The choice $\tau_P = nT$ defines the local *Pyragas curve* in the (λ, τ) plane for any $n \in \mathbb{N}$

$$\tau_P(\lambda) = \frac{2\pi n}{1 - \gamma\lambda} = 2\pi n(1 + \gamma\lambda + \dots), \tag{4.50}$$

which emanates from the Hopf bifurcation points $\lambda = 0,\ \tau = 2\pi n$.

Under further nondegeneracy conditions, the Hopf point $\lambda = 0$, $\tau = nT$ ($n \in \mathbb{N}_0$) continues to a Hopf bifurcation curve $\tau_H(\lambda)$ for $\lambda < 0$. We determine this *Hopf curve* next. It is characterized by purely imaginary eigenvalues $\eta = i\omega$ of the transcendental characteristic equation:

$$\eta = \lambda + i + b\left(e^{-\eta\tau} - 1\right), \tag{4.51}$$

which results from the linearization at the steady state $z = 0$ of the delayed system (4.47). Separating (4.51) into real and imaginary parts

$$0 = \lambda + b_0[\cos(\beta - \omega\tau) - \cos\beta] \tag{4.52}$$

$$\omega - 1 = b_0[\sin(\beta - \omega\tau) - \sin\beta] \tag{4.53}$$

and using trigonometric identities to eliminate $\omega(\lambda)$ yields an explicit expression for the multivalued Hopf curve $\tau_H(\lambda)$ for given control amplitude b_0 and phase β:

$$\tau_H = \frac{\pm \arccos\left(\frac{b_0 \cos\beta - \lambda}{b_0}\right) + \beta + 2\pi n}{1 - b_0 \sin\beta \pm \sqrt{\lambda(2b_0 \cos\beta - \lambda) + b_0^2 \sin^2\beta}}. \tag{4.54}$$

Note that τ_H is not defined in the case of $\beta = 0$ and $\lambda < 0$. Thus complex b is a necessary condition for the existence of the Hopf curve in the subcritical regime $\lambda < 0$. Figure 4.15 displays the family of Hopf curves (4.54), and the Pyragas curve (4.50) $n = 1$, in the (λ, τ) plane. In Fig. 4.15(b) the domains of instability of the trivial steady state $z = 0$, bounded by the Hopf curves, are marked by light gray shading (yellow). The dimensions of the unstable manifold of $z = 0$ are given in parentheses along the τ-axis in Fig. 4.15(b). By construction, the delay τ becomes a multiple of the minimum period T of the bifurcating periodic orbits along the Pyragas curve $\tau = \tau_p(\lambda) = nT$ and the time-delayed feedback term vanishes if the periodic orbit is stabilized. The inset of Fig. 4.16 displays the Hopf and Pyragas curves for different values of the feedback b_0. These choices of b_0 are displayed as full circles in the main figure. For $b_0 > b_0^{\text{crit}}$ (a) the Pyragas curve runs partly inside the Hopf curve. With decreasing magnitude of b_0 the Hopf curves pull back until the

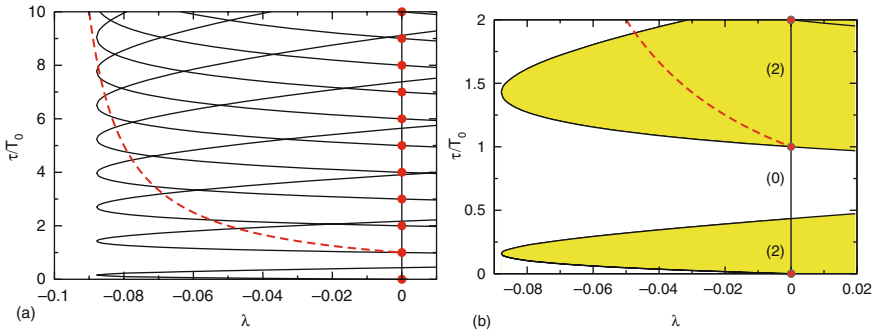

Fig. 4.15 Pyragas (*dashed*) and Hopf (*solid*) curves in the (λ, τ) plane: (**a**) Hopf bifurcation curves $n = 0, ..., 10$ and (**b**) Hopf bifurcation curves $n = 0, 1$ in an enlarged scale. *Light gray shading marks* the domains of unstable $z = 0$ and numbers in parentheses denote the dimension of the unstable manifold of $z = 0$ ($\gamma = -10$, $b_0 = 0.3$, and $\beta = \pi/4$). The time delay is given in units of the intrinsic timescale T_0 of the trivial fixed point, i.e., $T_0 = 2\pi$ [52]

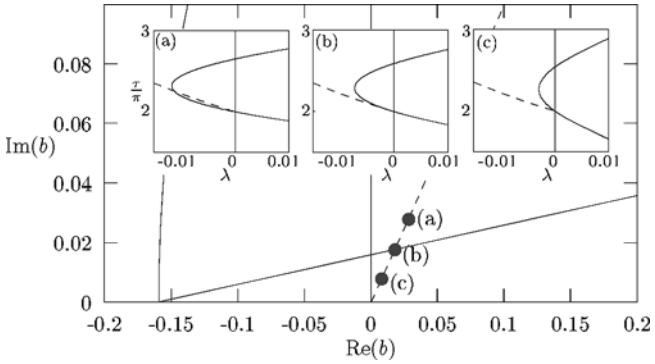

Fig. 4.16 Change of Hopf curves with varying control amplitude b_0. The main figures shows the complex plane of control gain b. The three values marked by *full circles* correspond to the insets (**a**), (**b**), and (**c**), where the Hopf (*solid*) and Pyragas (*dashed*) curves are displayed for $\beta = \frac{\pi}{4}$ and three different choices of b_0: (a) $b_0 = 0.04 > b_0^{\text{crit}}$, (b)$b_0 = 0.025 \approx b_0^{\text{crit}}$, and (c) $b_0 = 0.01 < b_0^{\text{crit}}$ ($\lambda = -0.005$, $\gamma = -10$) [130]

Pyragas curves lie outside (c). At the critical feedback value (b) Pyragas and Hopf curves are tangent at ($\lambda = 0, \tau = 2\pi$).

Standard exchange of stability results [131], which hold verbatim for delay equations, then assert that the bifurcating branch of periodic solutions locally inherits linear asymptotic (in)stability from the trivial steady state, i.e., it consists of stable periodic orbits on the Pyragas curve $\tau_P(\lambda)$ inside the shaded domains for small $|\lambda|$. We stress that an unstable trivial steady state is not a sufficient condition for stabilization of the Pyragas orbit. In fact, the stabilized Pyragas orbit can become unstable again if $\lambda < 0$ is further decreased, for instance, in a torus bifurcation. However, there exists an interval for values of λ in our example for which the exchange of stability holds. More precisely, for small $|\lambda|$ unstable periodic orbits possess a single Floquet multiplier $\mu = \exp(\Lambda\tau)$ (with $1 < \mu < \infty$), near unity, which is simple. All other nontrivial Floquet multipliers lie strictly inside the complex unit circle. In particular, the (strong) unstable dimension of these periodic orbits is odd, here 1, and their unstable manifold is two-dimensional. This is shown in Fig. 4.17 panel (a) top, which depicts solutions Λ of the characteristic equation of the periodic solution on the Pyragas curve.

The Floquet exponents of the Pyragas orbit can be calculated explicitly by rewriting (4.47) in polar coordinates $z = r\, e^{i\theta}$

$$\dot{r} = (\lambda + r^2)\, r + b_0[\cos(\beta + \theta(t-\tau) - \theta)\, r(t-\tau) - \cos(\beta)\, r] \tag{4.55}$$

$$\dot{\theta} = 1 + \gamma r^2 + b_0[\sin(\beta + \theta(t-\tau) - \theta)\, \frac{r(t-\tau)}{r} - \sin(\beta)] \tag{4.56}$$

and linearizing around the periodic orbit according to $r(t) = r_0 + \delta r(t)$ and $\theta(t) = \Omega t + \delta\theta(t)$, with $r_0 = \sqrt{-\lambda}$ and $\Omega = 1 - \gamma\lambda$ (see (4.48)). This yields

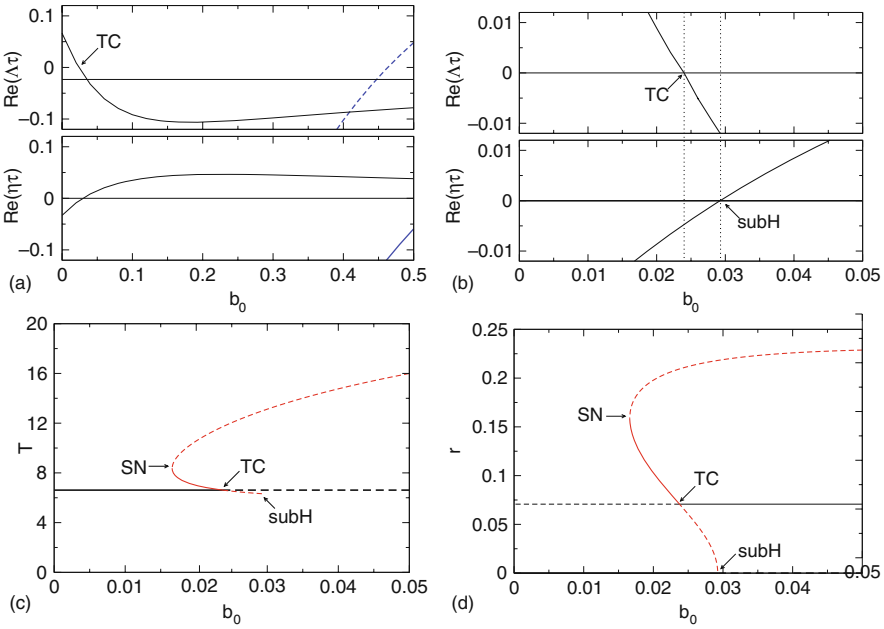

Fig. 4.17 (**a**) *Top*: real part of Floquet exponents Λ of the periodic orbit vs. feedback amplitude b_0. *Bottom*: real part of eigenvalue η of steady state vs. feedback amplitude b_0; (**b**) blowup of (**a**); (**c**) periods; and (**d**) radii of the periodic orbits vs. b_0. The *solid* and *dashed curves* correspond to stable and unstable periodic orbits, respectively. Parameters in all panels: $\lambda = -0.005$, $\gamma = -10$, $\tau = \frac{2\pi}{1-\gamma\lambda}$, and $\beta = \pi/4$ [130]

$$\begin{pmatrix} \dot{\delta r(t)} \\ \dot{\delta\theta(t)} \end{pmatrix} = \begin{bmatrix} -2\lambda - b_0 \cos\beta & b_0 r_0 \sin\beta \\ 2\gamma r_0 - b_0 \sin\beta\, r_0^{-1} & -b_0 \cos\beta \end{bmatrix} \begin{pmatrix} \delta r(t) \\ \delta\theta(t) \end{pmatrix} \tag{4.57}$$

$$+ \begin{bmatrix} b_0 \cos\beta & -b_0 r_0 \sin\beta \\ b_0 \sin\beta r_0^{-1} & b_0 \cos\beta \end{bmatrix} \begin{pmatrix} \delta r(t-\tau) \\ \delta\theta(t-\tau) \end{pmatrix}. \tag{4.58}$$

With the ansatz

$$\begin{pmatrix} \delta r(t) \\ \delta\theta(t) \end{pmatrix} = u\ \exp(\Lambda t), \tag{4.59}$$

where u is a two-dimensional vector, one obtains the autonomous linear equation

$$\begin{bmatrix} -2\lambda + b_0 \cos\beta\,(e^{-\Lambda\tau} - 1) - \Lambda & -b_0 r_0 \sin\beta\,(e^{-\Lambda\tau} - 1) \\ 2\gamma r_0 + b_0 r_0^{-1} \sin\beta\,(e^{-\Lambda\tau} - 1) & b_0 \cos\beta\,(e^{-\Lambda\tau} - 1) - \Lambda \end{bmatrix} u = 0. \tag{4.60}$$

The condition of vanishing determinant then gives the transcendental characteristic equation:

$$0 = \left(-2\lambda + b_0 \cos\beta\,(e^{-\Lambda\tau} - 1) - \Lambda\right)\left(b_0 \cos\beta\,(e^{-\Lambda\tau} - 1) - \Lambda\right) \quad (4.61)$$

$$-b_0 r_0 \sin\beta\,(e^{-\Lambda\tau} - 1)\left(2\gamma r_0 + b_0 r_0^{-1} \sin\beta\,(e^{-\Lambda\tau} - 1)\right) \quad (4.62)$$

for the Floquet exponents Λ which can be solved numerically.

The largest real part is positive for $b_0 = 0$. Thus the periodic orbit is unstable. As the amplitude of the feedback gain increases, the largest real part of the eigenvalue becomes smaller and eventually changes sign at the point TC (transcritical bifurcation) in Fig. 4.17. Hence the periodic orbit is stabilized. Note that an infinite number of Floquet exponents are created by the control scheme; their real parts tend to $-\infty$ in the limit $b_0 \to 0$, and some of them may cross over to positive real parts for larger b_0 (dashed line in Fig. 4.17(a)), terminating the stability of the periodic orbit.

Panel (a) bottom illustrates the stability of the steady state by displaying the largest real part of the eigenvalues η. The interesting region of the top and bottom panels where the periodic orbit becomes stable and the fixed point loses stability is magnified in panel (b).

Figure 4.18 shows the behavior of the Floquet multipliers $\mu = \exp(\Lambda\tau)$ of the Pyragas orbit in the complex plane with the increasing amplitude of the feedback gain b_0 as a parameter (marked by arrows). There is an isolated real multiplier crossing the unit circle at $\mu = 1$. This is caused by a transcritical bifurcation in which the Pyragas orbit collides with a delay-induced stable periodic orbit. In panels (c) and (d) of Fig. 4.17 the periods and radii of all circular periodic orbits ($r = \text{const}$) are plotted vs. the feedback strength b_0. For small b_0 only the initial (unstable) Pyragas orbit (T and r independent of b_0) and the steady state $r = 0$ (stable) exist. With increasing b_0 a pair of unstable/stable periodic orbits is created in a saddle-node (SN) bifurcation. The stable one of the two orbits (solid) then exchanges stability with the Pyragas orbit in a transcritical bifurcation (TC), and finally ends in a

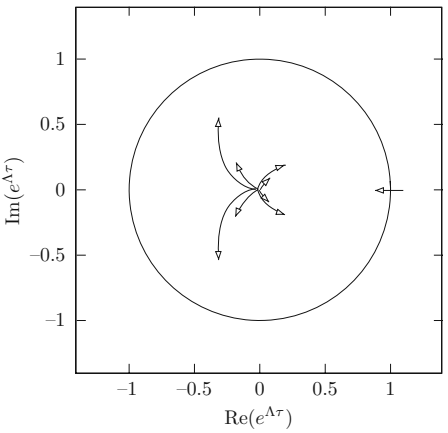

Fig. 4.18 Floquet multipliers $\mu = \exp(\Lambda\tau)$ in the complex plane with the feedback amplitude $b_0 \in [0, 0.3]$. *Arrows* indicate the direction of increasing b_0. Same parameters as in Fig. 4.17 [130]

subcritical Hopf bifurcation (subH), where the steady state $r = 0$ becomes unstable. The Pyragas orbit continues as a stable periodic orbit for larger b_0. Except at TC, the delay-induced orbit has a period $T \neq \tau$ (see Fig. 4.17c). Note that the respective exchanges of stability of the Pyragas orbit (TC) and the steady state (subH) occur at slightly different values of b_0. This is also corroborated by Fig. 4.17(b). The mechanism of stabilization of the Pyragas orbit by a transcritical bifurcation relies upon the possible existence of such delay-induced periodic orbits with $T \neq \tau$, which was overlooked in previous works. Technically, the proof of the odd number limitation theorem in [44] fails because the trivial Floquet multiplier $\mu = 1$ (Goldstone mode of periodic orbit) was neglected there; $F(1)$ in (14) in [44] is thus zero and not less than zero, as assumed. At TC, where a second Floquet multiplier crosses the unit circle, this results in a Floquet multiplier $\mu = 1$ of algebraic multiplicity two.

Next we analyze the conditions under which stabilization of the subcritical periodic orbit is possible. From Fig. 4.15(b) it is evident that the Pyragas curve must lie inside the yellow region, i.e., the Pyragas and Hopf curves emanating from the point $(\lambda, \tau) = (0, 2\pi)$ must locally satisfy the inequality $\tau_H(\lambda) < \tau_P(\lambda)$ for $\lambda < 0$. More generally, let us investigate the eigenvalue crossings of the Hopf eigenvalues $\eta = i\omega$ along the τ-axis of Fig. 4.15. In particular, we derive conditions for the unstable dimensions of the trivial steady state near the Hopf bifurcation point $\lambda = 0$ in our model (4.47). On the τ-axis ($\lambda = 0$), the characteristic equation (4.51) for $\eta = i\omega$ is reduced to

$$\eta = i + b\left(e^{-\eta\tau} - 1\right), \tag{4.63}$$

and we obtain two series of Hopf points given by

$$0 \leq \tau_n^A = 2\pi, n \tag{4.64}$$

$$0 < \tau_n^B = \frac{2\beta + 2\pi n}{1 - 2b_0 \sin\beta} \quad (n = 0, 1, 2, \dots). \tag{4.65}$$

The corresponding Hopf frequencies are $\omega^A = 1$ and $\omega^B = 1 - 2b_0 \sin\beta$, respectively. Note that series A consists of all Pyragas points, since $\tau_n^A = nT = 2\pi n/\omega^A$. In the series B the integers n have to be chosen such that the delay $\tau_n^B \geq 0$. The case $b_0 \sin\beta = 1/2$, only, corresponds to $\omega^B = 0$ and does not occur for finite delays τ.

We evaluate the crossing directions of the critical Hopf eigenvalues next, along the positive τ-axis and for both series. Abbreviating $\frac{\partial}{\partial\tau}\eta$ by η_τ the crossing direction is given by sign(Re η_τ). Implicit differentiation of (4.63) with respect to τ at $\eta = i\omega$ implies

$$\text{sign}(\text{Re}\ \eta_\tau) = -\text{sign}(\omega)\,\text{sign}(\sin(\omega\tau - \beta)). \tag{4.66}$$

We are interested specifically in the Pyragas–Hopf points of series A (marked by dots in Fig. 4.15), where $\tau = \tau_n^A = 2\pi n$ and $\omega = \omega^A = 1$. Indeed sign(Re η_τ) = sign($\sin\beta$) > 0 holds, provided we assume $0 < \beta < \pi$, i.e., $b_I > 0$ for the

feedback gain. This condition alone, however, is not sufficient to guarantee stability of the steady state for $\tau < 2n\pi$. We also have to consider the crossing direction sign(Re η_τ) along series B, $\omega^B = 1 - 2b_0 \sin\beta$, $\omega^B \tau_n^B = 2\beta + 2\pi n$, for $0 < \beta < \pi$. Equation (4.66) now implies sign(Re η_τ) = sign$((2b_0 \sin\beta - 1)\sin\beta)$ = sign$(2b_0 \sin\beta - 1)$.

To compensate for the destabilization of $z = 0$ upon each crossing of any point $\tau_n^A = 2\pi n$, we must require stabilization (sign(Re η_τ) < 0) at each point τ_n^B of series B. If $b_0 \geq 1/2$, this requires $0 < \beta < \arcsin(1/(2b_0))$ or $\pi - \arcsin(1/(2b_0)) < \beta < \pi$. The distance between two successive points τ_n^B and τ_{n+1}^B is $2\pi/\omega^B > 2\pi$. Therefore, there is at most one τ_n^B between any two successive Hopf points of series A. Stabilization requires exactly one such τ_n^B, specifically: $\tau_{k-1}^A < \tau_{k-1}^B < \tau_k^A$ for all $k = 1, 2, \ldots, n$. This condition is satisfied if, and only if,

$$0 < \beta < \beta_n^*, \tag{4.67}$$

where $0 < \beta_n^* < \pi$ is the unique solution of the transcendental equation:

$$\frac{1}{\pi}\beta_n^* + 2nb_0 \sin\beta_n^* = 1. \tag{4.68}$$

This holds because the condition $\tau_{k-1}^A < \tau_{k-1}^B < \tau_k^A$ first fails when $\tau_{k-1}^B = \tau_k^A$. Equation (4.67) represents a necessary but not yet sufficient condition that the Pyragas choice $\tau_P = nT$ for the delay time will stabilize the periodic orbit.

To evaluate the remaining condition, $\tau_H < \tau_P$ near $(\lambda, \tau) = (0, 2\pi)$, we expand the exponential in the characteristic equation (4.51) for $\omega\tau \approx 2\pi n$, and obtain the approximate Hopf curve for small $|\lambda|$:

$$\tau_H(\lambda) \approx 2\pi n - \frac{1}{b_I}(2\pi n b_R + 1)\lambda. \tag{4.69}$$

Recalling (4.50), the Pyragas stabilization condition $\tau_H(\lambda) < \tau_P(\lambda)$ is therefore satisfied for $\lambda < 0$ if, and only if,

$$\frac{1}{b_I}\left(b_R + \frac{1}{2\pi n}\right) < -\gamma. \tag{4.70}$$

Equation (4.70) defines a domain in the plane of the complex feedback gain $b = b_R + ib_I = b_0 e^{i\beta}$ bounded from below (for $\gamma < 0 < b_I$) by the straight line

$$b_I = \frac{1}{-\gamma}\left(b_R + \frac{1}{2\pi n}\right). \tag{4.71}$$

Equation (4.68) represents a curve $b_0(\beta)$, i.e.,

$$b_0 = \frac{1}{2n \sin\beta}\left(1 - \frac{\beta}{\pi}\right), \tag{4.72}$$

which forms the upper boundary of a domain given by the inequality (4.67). Thus (4.71) and (4.72) describe the boundaries of the domain of control in the complex plane of the feedback gain b in the limit of small λ. Figure 4.19 depicts this domain of control for $n = 1$, i.e., a time delay $\tau = \frac{2\pi}{1-\gamma\lambda}$. The lower and upper solid curves correspond to (4.71) and (4.72), respectively. The grayscale displays the numerical result of the largest real part, wherever negative, of the Floquet exponent, calculated from linearization of the amplitude and phase equations around the periodic orbit. Outside the shaded areas the periodic orbit is not stabilized. With increasing $|\lambda|$ the domain of stabilization shrinks, as the deviations from the linear approximation (4.69) become larger. For sufficiently large $|\lambda|$ stabilization is no longer possible in agreement with Fig. 4.15(b). Note that for real values of b, i.e., $\beta = 0$, no stabilization occurs at all. Hence, stabilization fails if the feedback matrix B is a multiple of the identity matrix. Figure 4.20 compares the control domain for the same value of $|\lambda|$ for the representation in the planes of complex feedback b (left) and amplitude b_0 and phase β (right).

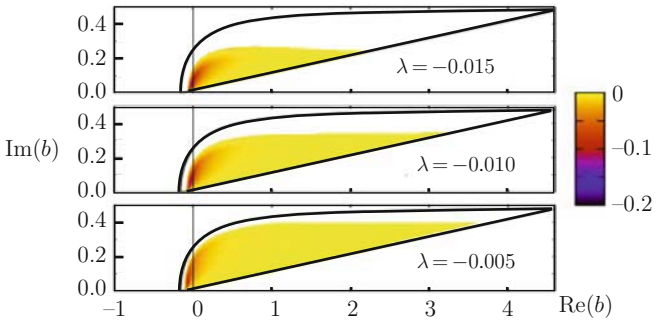

Fig. 4.19 Domain of control in the plane of the complex feedback gain $b = b_0 e^{i\beta}$ for three different values of the bifurcation parameter λ. The *solid curves* indicate the boundary of stability in the limit $\lambda \nearrow 0$, see (4.71) and (4.72). The *shading* shows the magnitude of the largest (negative) real part of the Floquet exponents of the periodic orbit ($\gamma = -10$ and $\tau = \frac{2\pi}{1-\gamma\lambda}$) [52]

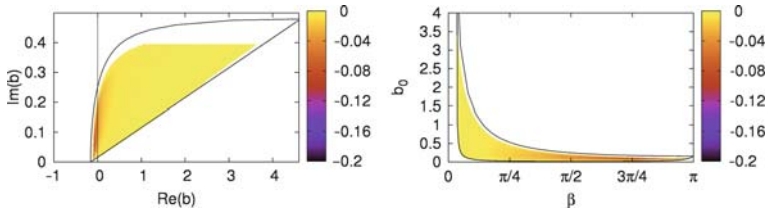

Fig. 4.20 Domain of control in the complex b plane (*left*) and the (β, b_0) plane (*right*) ($\lambda = -0.005$, $\gamma = -10$, and $\tau = \frac{2\pi}{1-\gamma\lambda}$) [130]

4.2.4 Stabilizing Periodic Orbits Near a Fold Bifurcation

Another important example for an unstable periodic orbit which has an odd number of real Floquet multipliers greater than unity is provided by an orbit generated by a fold bifurcation of limit cycles. As a paradigm for fold bifurcation of rotating waves we consider planar systems of the form

$$\dot{z} = g(\lambda, |z|^2)z + ih(\lambda, |z|^2)z. \tag{4.73}$$

Here $z(t)$ is a scalar complex variable, g and h are real valued functions, and λ is a real parameter. Systems of the form (4.73) are S^1 equivariant, i.e., $e^{i\theta}z(t)$ is a solution whenever $z(t)$ is for any fixed $e^{i\theta}$ in the unit circle S^1. In polar coordinates $z = re^{i\varphi}$, this manifests itself by the absence of φ from the right-hand sides of the resulting differential equations:

$$\begin{aligned} \dot{r} &= g(\lambda, r^2)r, \\ \dot{\varphi} &= h(\lambda, r^2). \end{aligned} \tag{4.74}$$

In particular, all periodic solutions of (4.73) are indeed rotating waves, alias harmonic, of the form

$$z(t) = re^{i\omega t}$$

for suitable nonzero real constants r, ω. Specifically, this requires $\dot{r} = 0$ and $\dot{\varphi} = \omega$:

$$\begin{aligned} 0 &= g(\lambda, r^2), \\ \omega &= h(\lambda, r^2). \end{aligned} \tag{4.75}$$

Fold bifurcations of rotating waves are generated by the nonlinearities

$$\begin{aligned} g(\lambda, r^2) &= \left(r^2 - 1\right)^2 - \lambda, \\ h(\lambda, r^2) &= \gamma(r^2 - 1) + \omega_0. \end{aligned} \tag{4.76}$$

Our choice of nonlinearities is generic in the sense that $g(\lambda, r^2)$ is the normal form for a nondegenerate fold bifurcation [132] at $r^2 = 1$ and $\lambda = 0$. See Fig. 4.21 for the resulting bifurcation diagram. We fix coefficients $\gamma, \omega_0 > 0$.

Using (4.75) and (4.76), the amplitude r and frequency ω of the rotating waves then satisfy

$$r^2 = 1 \pm \sqrt{\lambda}, \quad \omega = \omega_0 + \gamma(r^2 - 1) = \omega_0 \pm \gamma\sqrt{\lambda}. \tag{4.77}$$

The signs $\pm$ correspond to different branches in Fig. 4.21, $+$ unstable and $-$ stable.

Our goal is to investigate delay stabilization of the fold system (4.73) by the delayed feedback term

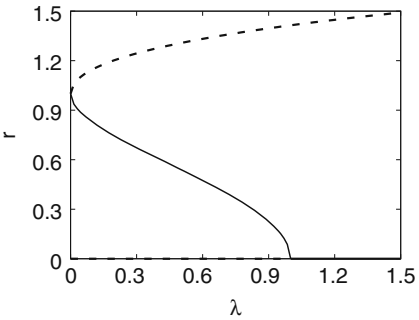

Fig. 4.21 Bifurcation diagram of rotating waves (*solid line*: stable; *dashed line*: unstable) of (4.73) and (4.76) [54]

$$\dot{z} = f(\lambda, |z|^2)z + b_0 e^{i\beta}\left[z(t-\tau) - z(t)\right], \tag{4.78}$$

with real positive control amplitude b_0, delay τ, and real control phase β. Here we have used the abbreviation $f = g + ih$. The Pyragas choice requires the delay τ to be an integer multiple k of the minimum period T of the periodic solution to be stabilized:

$$\tau = kT. \tag{4.79}$$

This choice guarantees that periodic orbits of the original system (4.73) with period T are reproduced exactly and non-invasively by the control system (4.78). The minimum period T of a rotating wave $z = re^{i\omega t}$ is given explicitly by $T = 2\pi/\omega$. Using (4.77), (4.79) becomes

$$\tau = \frac{2\pi k}{\omega_0 \pm \gamma\sqrt{\lambda}}, \tag{4.80}$$

or, equivalently,

$$\lambda = \lambda(\tau) = \left(\frac{2\pi k - \omega_0\tau}{\gamma\tau}\right)^2. \tag{4.81}$$

In the following we select only the branch of $\lambda(\tau)$ corresponding to the τ value with the $+$ sign, which is associated with the unstable orbit. Condition (4.81) then determines the kth *Pyragas curve* in parameter space (τ, λ) where the delayed feedback is indeed non-invasive. The fold parameter $\lambda = 0$ corresponds to $\tau = 2\pi k/\omega_0$ along the kth Pyragas curve. See Fig. 4.22 for the Pyragas curves in the parameter plane (τ, λ).

For the delay stabilization system (4.78) we now consider τ as the relevant bifurcation parameter. We restrict our study of (4.78) to $\lambda = \lambda(\tau)$ given by the Pyragas

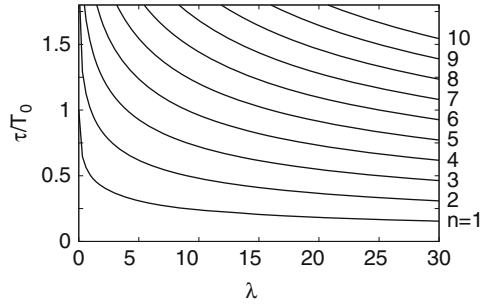

Fig. 4.22 The Pyragas curves $\lambda = \lambda(\tau)$, corresponding to the unstable branch in Fig. 4.21, in the parameter plane (τ, λ); see (4.81). Parameters: $\gamma = \omega_0 = 1$ [54]

curve (4.81), because $\tau = kT$ is the primary condition for non-invasive delayed feedback control.

We begin with the trivial case $b_0 = 0$ of vanishing control. For each $\lambda = \lambda(\tau)$, we encounter two rotating waves given by

$$r^2 = 1 \pm \frac{2\pi k - \omega_0 \tau}{\gamma \tau}, \quad \omega = \omega_0 \pm \left(\frac{2\pi k - \omega_0 \tau}{\tau} \right). \tag{4.82}$$

The two resulting branches form a transcritical bifurcation at $\tau = 2\pi k/\omega_0$. At this stage, the transcriticality looks like an artifact, spuriously caused by our choice of the Pyragas curve $\lambda = \lambda(\tau)$. Note, however, that only one of the two crossing branches features minimum period T such that the Pyragas condition $\tau = kT$ holds. This happens along the branch

$$r^2 = 1 + \frac{2\pi k - \omega_0 \tau}{\gamma \tau}, \quad \omega = 2\pi k/\tau,$$

see Fig. 4.23. We call this branch, which corresponds to '+' in (4.82) the *Pyragas branch*. The other branch has minimum period T with

$$kT = \frac{\pi k}{\omega_0 \tau - \pi k} \tau \neq \tau,$$

except at the crossing point $\omega_0 \tau = 2\pi k$. The minus branch therefore violates the Pyragas condition for non-invasive control, even though it has been generated from the same fold bifurcation.

Our strategy for Pyragas control of the unstable part of the Pyragas branch is now simple. For a nonzero control amplitude b_0, the Pyragas branch persists without change, due to the non-invasive property $\tau = kT$ along the Pyragas curve $\lambda = \lambda(\tau)$. The minus branch, however, will be perturbed slightly for small $b_0 \neq 0$. If the resulting perturbed transcritical bifurcation

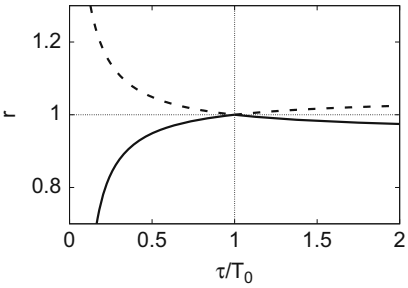

Fig. 4.23 Bifurcation diagram of rotating waves of (4.78) at vanishing control amplitude $b_0 = 0$. Parameters: $T_0 = 2\pi/\omega_0$, $\omega_0 = 1$, and $\gamma = 10$ [54]

$$\tau = \tau_c \tag{4.83}$$

moves to the left, i.e., below $2\pi k/\omega_0$, then the stability region of the Pyragas branch has invaded the unstable region of the fold bifurcation. Again this refutes the notorious odd number limitation of Pyragas control, see Fiedler et al. [52] and references therein.

Let $\tau = \tau_c$ denote the transcritical bifurcation point on the Pyragas curve $\lambda = \lambda(\tau)$, see (4.81). Let $z(t) = r_c e^{i\omega_c t}$ denote the corresponding rotating wave and abbreviate $\varepsilon \equiv r_c^2 - 1$. Conditions for the transcritical bifurcation in (4.78) can be obtained [54], which yield the following relations between the control amplitude b_c at the bifurcation and ε, τ_c:

$$b_c = -\varepsilon \frac{\omega_0 + \gamma\varepsilon}{k\pi(\gamma \sin\beta + 2\varepsilon\cos\beta)} \tag{4.84}$$

and

$$b_c = -\frac{2\pi k - \omega_0\tau_c}{\tau_c\left(\frac{1}{2}\gamma^2\tau_c \sin\beta + (2\pi k - \omega_0\tau_c)\cos\beta\right)}. \tag{4.85}$$

As follows from (4.84) and (4.85), for small ε, alias for τ_c near $2k\pi/\omega_0$, the optimal control angle is $\beta = -\pi/2$ in the limit $\varepsilon \to 0$, and for fixed $k, \omega_0, \gamma, \varepsilon$ this control phase β allows for stabilization with the smallest amplitude $|b_c|$. For $\beta = -\pi/2$ the relations (4.84) and (4.85) simplify to

$$b_c = \frac{\varepsilon}{k\pi}\left(\frac{\omega_0}{\gamma} + \varepsilon\right) \tag{4.86}$$

and

$$b_c = \frac{2}{(\gamma\tau_c)^2}\left(2k\pi - \omega_0\tau_c\right), \tag{4.87}$$

respectively. For small $b_0 > 0$ we also have the expansions

$$\varepsilon = -\left(k\pi \frac{\gamma}{\omega_0} \sin\beta\right) b_0 + \cdots \tag{4.88}$$

and

$$\tau_c = \frac{2\pi k}{\omega_0} + \left(\frac{1}{2\omega_0}\left(\frac{2k\pi\gamma}{\omega_0}\right)^2 \sin\beta\right) b_0 + \cdots . \tag{4.89}$$

for the location of the transcritical bifurcation. In particular, we see that odd number delay stabilization can be achieved by arbitrary small control amplitudes b_0 near the fold for $\gamma > 0$ and $\sin\beta < 0$. Note that the stability region of the Pyragas curve increases if $\varepsilon = r_c^2 - 1 > 0$, see Fig. 4.21. For vanishing phase angle of the control, $\beta = 0$, in contrast, delay stabilization cannot be achieved by arbitrarily small control amplitudes b_0 near the fold in our system (4.78).

Even far from the fold at $\lambda = 0$ and $\tau = 2k\pi/\omega_0$ the above formulas (4.84), (4.86), and (4.87) hold and indicate a transcritical bifurcation from the (global) Pyragas branch of rotating waves of (4.78) along the Pyragas curve $\lambda = \lambda(\tau)$. This follows by analytic continuation. Delay stabilization, however, may fail long before $\tau = \tau_c$ is reached. In fact, nonzero purely imaginary Floquet exponents may arise, which destabilize the Pyragas branch long before $\tau = \tau_c$ is reached. This interesting point remains open.

A more global picture of the orbits involved in the transcritical bifurcation may be obtained by numerical analysis. Rewriting (4.78) in polar coordinates $z = re^{i\varphi}$ yields

$$\dot{r} = [(r^2-1)^2 - \lambda]r + b_0[\cos(\beta + \varphi(t-\tau) - \varphi)\, r(t-\tau) - r\cos\beta] \tag{4.90}$$

$$\dot{\varphi} = \gamma(r^2-1) + \omega_0 + b_0[\sin(\beta + \varphi(t-\tau) - \varphi)\, r(t-\tau)/r - \sin\beta]. \tag{4.91}$$

To find all rotating wave solutions we make the ansatz $r = \text{const}$ and $\dot{\varphi} = \omega = \text{const}$ and obtain

$$0 = (r^2-1)^2 - \lambda + b_0[\cos(\beta - \omega\tau) - \cos\beta] \tag{4.92}$$

$$\omega = \gamma(r^2-1) + \omega_0 + b_0[\sin(\beta - \omega\tau) - \sin\beta]. \tag{4.93}$$

Eliminating r we find a transcendental equation for ω

$$0 = -\gamma^2\lambda + \gamma^2 b_0[\cos(\beta - \omega\tau) - \cos\beta] \tag{4.94}$$

$$+ (\omega - \omega_0 - b_0[\sin(\beta - \omega\tau) - \sin\beta])^2 . \tag{4.95}$$

One can now solve this equation numerically for ω and insert the result into

$$r = \left(\frac{\omega - \omega_0}{\gamma} - \frac{b_0}{\gamma} [\sin(\beta - \omega\tau) - \sin\beta] + 1 \right)^{\frac{1}{2}} \tag{4.96}$$

to obtain the allowed radii (discarding imaginary radii).

The orbit which stabilizes the Pyragas branch in the transcritical bifurcation may be the minus branch or another delay-induced orbit which is born in a fold bifurcation, depending on the parameters. Figure 4.24 displays the different scenarios and the crossover in dependence on the control amplitude b_0. The value of γ is chosen as $\gamma = 9$, 10.5, 10.6, and 13 in panels (a), (b), (c), and (d), respectively. It can be seen that the Pyragas orbit is stabilized by a transcritical bifurcation T_1. As the value of γ increases, a pair of a stable and an unstable orbit generated by a fold bifurcation F_1 approaches the minus branch (see Fig. 4.24a). On this branch, fold bifurcations (F_2 and F_3) occur as shown in Fig. 4.24(b). At $\gamma = 10.6$, the fold points of F_1 and F_2 touch in a transcritical bifurcation T_2 and annihilate (see Fig. 4.24(c, d). Thus, for further increase of γ, one is left with the stable minus branch and the unstable orbit, which was generated at the fold bifurcation F_3. In all panels the radius of the Pyragas orbit is not changed by the control. The radius of the minus branch, however, is altered because the delay time does not match orbit period.

Figure 4.25 shows the region in the (β, b_0) plane where the Pyragas orbit is stable, for a set of parameters. The grayscale (color code) shows only negative values of the largest real part of the Floquet exponents. One can see that the orbit is most stable for feedback phases $\beta \approx -\pi/2$ which agrees with the previous analytic

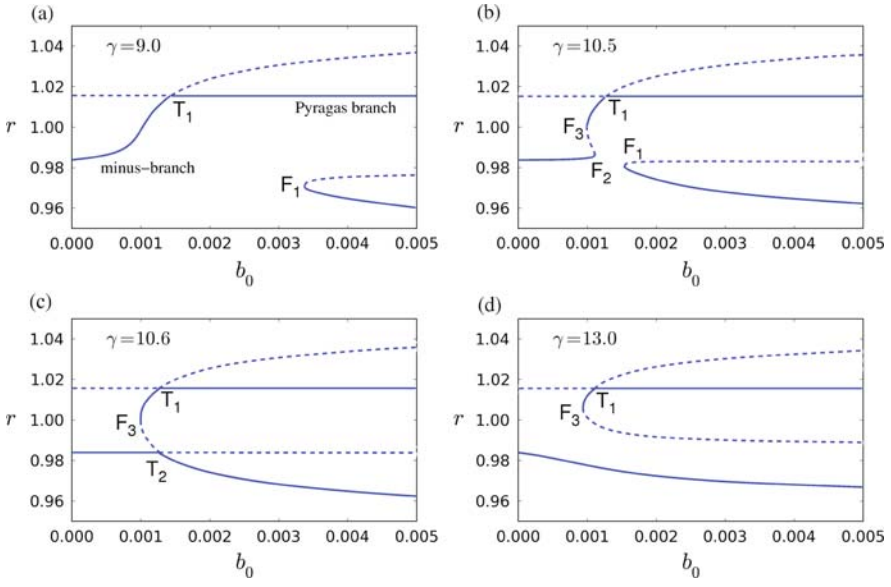

Fig. 4.24 Radii of stable (*solid*) and unstable (*dashed*) rotating wave solutions in dependence on b_0 for different γ. Parameters: $\omega_0 = 1$, $\lambda = 0.001$, and $\beta = -\pi/2$ [54]

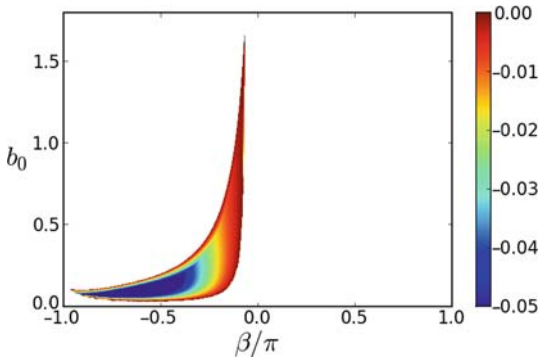

Fig. 4.25 Domain of stability of the Pyragas orbit. The *grayscale* (*color code*) shows only negative values of the largest real part of the Floquet exponents. Parameters: $\omega_0 = 1$, $\lambda = 0.0001$, and $\gamma = 0.1$. [54]

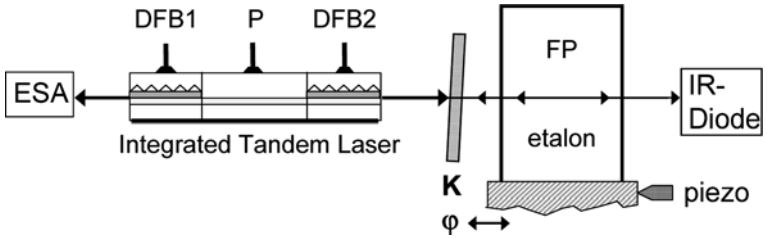

Fig. 4.26 Scheme of an integrated tandem laser with optical feedback from an external Fabry–Perot etalon. Two distributed feedback (DFB) lasers are connected via a passive waveguide section P. Amplitude K and phase φ of the feedback from the FP resonator are controlled by a variable neutral density filter and a piezo positioning, respectively. ESA: electrical spectrum analyzer. IR Diode: power measurement [38]

results for small λ. The picture was obtained by linear stability analysis of (4.90) and (4.91) and numerical solution of the transcendental eigenvalue problem for the Floquet exponents. It clearly shows that the periodic orbit can be stabilized even though it has an odd number of real Floquet multipliers greater than unity.

These results of the simple normal form model can be transferred to a more realistic model of an integrated tandem laser [54], such as the one considered in the next section, see Fig. 4.26, where time-delayed feedback control is realized by a Michelson interferometer.

4.3 Time-Delayed Control of Optical Systems

In this section we will consider semiconductor lasers, where time-delayed feedback control can be readily realized by optical feedback from a mirror or a Fabry–Perot (FP) resonator, and this allows for controlling systems with very fast dynamics still in real-time mode.

4.3.1 Stabilizing Continuous-Wave Laser Emission by Phase-Dependent Coupling

From a practical point of view, it is often desirable to suppress self-sustained oscillations, i.e., intensity pulsations, in order to stabilize continuous-wave (cw) operation of lasers [133, 134]. This amounts to stabilizing an unstable fixed point of the dynamic laser equations.

Here we consider a semiconductor laser device for which control of unstable steady states by time-delayed feedback control has been demonstrated in theory and experiment [38]. Recently, multi-section lasers with their complex dynamical phenomena have opened up new ways in high-speed optical information processing [135, 136]. Their picosecond response times are too short even for a fast electronic realization of time-delayed feedback control. All-optical control is thus the only applicable method so far. The scheme of the setup is shown in Fig. 4.26. An integrated tandem laser [135, 136] is deliberately driven through a Hopf bifurcation into a self-pulsating regime of operation. Suppression of the pulsations and non-invasive stabilization of the steady state is achieved by direct optical feedback from a properly designed external FP etalon. Although proposed one and a half decades ago [39, 137] and despite of some numerical studies [137–139], such non-invasive all-optical control approach has not been implemented experimentally until recently [38]. A novel aspect of our analysis is that it addresses the role of the optical phase as a specific feature of the FP control configuration.

Optical fields emitted by lasers vary generally as $\mathrm{Re}\{E(t)e^{-i\omega_0 t}\}$ where the exponential factor oscillates by orders of magnitude faster than the slow amplitude $E(t)$. The field fed back from the FP resonator has the same shape and, for feedback gain K, its amplitude reads as

$$E_\mathrm{b}(t) = Ke^{i\varphi}\sum_{n=0}^{\infty} R^n e^{in\phi}[E(t_n) - e^{i\phi}E(t_{n+1})], \tag{4.97}$$

with $t_n = t - \tau_l - n\tau$. The delay originates from a single roundtrip between laser and FP resonator, characterized by the latency time τ_l, and n round-trips of time τ within the FP resonator of mirror reflectivity R. Two optical phase shifts $\varphi = \omega_0\tau_l$ and $\phi = \omega_0\tau$ are associated with these delay times. Non-invasive control requires optical target states with $E(t) = e^{i\phi}E(t-\tau)$. Feedback from a FP resonator has been studied previously, see, e.g., [140–143] and references therein. However, those configurations rely on maximum feedback are thus strongly invasive.

For steady states $E(t) = E_0$ non-invasiveness means $e^{i\phi} = 1$, i.e., the FP resonator must be tuned into resonance. While the FP phase is thus fixed, the latency is still arbitrary and makes the feedback phase-sensitive. Conventional time-delayed feedback control corresponds to $\varphi = 0$. However, in the FP geometry, φ is tunable by sub-wavelength changes of the laser-FP separation and thus represents an additional free parameter which all-optical time-delayed feedback control can profit from. In what follows, this is theoretically demonstrated within the simple generic

two-variable center-manifold model introduced in Sect. 4.2 [48]. Stabilization of the cw emission has also been shown within a more specific semiconductor laser model of Lang–Kobayashi type, including latency, bandpass filtering in the control loop, and a feedback phase [144].

We consider a nonlinear system closely above a Hopf bifurcation, where it has an unstable fixed point (focus) whose stability is governed by the complex eigenvalues $\lambda \pm i\omega$ (with $\lambda > 0$). For simplicity, we restrict ourself to a single FP roundtrip (n=1) and ignore τ_l in the slow amplitude dynamics. An extension to multiple time feedback (ETDAS) is found elsewhere [50]. Linearizing around the fixed point provides a generic equation for the center-manifold coordinates x, y, corresponding to the complex field through $E = E_0 + x + iy$,

$$\begin{pmatrix} \dot{x} \\ \dot{y} \end{pmatrix} = \begin{pmatrix} \lambda & \omega \\ -\omega & \lambda \end{pmatrix} \begin{pmatrix} x \\ y \end{pmatrix} - K \begin{pmatrix} \cos\varphi & -\sin\varphi \\ \sin\varphi & \cos\varphi \end{pmatrix} \begin{pmatrix} x(t) - x(t-\tau) \\ y(t) - y(t-\tau) \end{pmatrix}. \tag{4.98}$$

This equation generalizes the model of (4.6) to phase-sensitive feedback and shows that such feedback creates non-diagonal coupling terms [145]. The characteristic equation for the complex eigenvalues Λ reads as

$$\Lambda + Ke^{\pm i\varphi}\left(1 - e^{-\Lambda\tau}\right) = \lambda \pm i\omega. \tag{4.99}$$

Note that this characteristic equation can be solved analytically using the Lambert function, which is defined as the inverse function of $g(z) = ze^z$ for complex z.

Figure 4.27 shows the domain of control, i.e., $\mathrm{Re}(\Lambda) < 0$, in dependence on the parameters φ, K, and τ. Unit of time is the intrinsic period $T_0 = 2\pi/\omega$ of the unstable focus and $\lambda T_0 = 0.2$ is chosen in all plots. Panels (a) and (b) represent the (φ, K) plane for fixed values of the time delay $\tau/T_0 = 0.5$ and 0.9, respectively. Note that $\tau = T_0/2$ yields a symmetric domain of control with respect to $\varphi = 0$, which is the case of diagonal coupling [48]. For values other than this optimal time delay, the domain of control is distorted and shrinks. In the situation shown in Fig. 4.27 (b), control can no longer be achieved for $\varphi = 0$, but only for positive phase $\varphi > 0$. Panels (c) and (d) show the domain of control in the (φ, τ) plane for fixed feedback gain $KT_0 = 1$ and 2, respectively. It consists of isolated islands with a horizontal extension that becomes maximum and symmetric with respect to $\varphi = 0$ at delays of $\tau = (n + 1/2)T_0$ ($n = 0, 1, 2, \ldots$). No control is possible for integer τ/T_0. For a range of τ values in between, stabilization can be achieved by appropriately chosen φ. When crossing the islands at fixed φ, resonance-type behavior of the damping rate $-\mathrm{Re}(\Lambda)$ occurs. With increasing n, the size of the islands decreases so that they eventually disappear at some critical value determined by the feedback strength K.

These results from the simple generic model have been confirmed by experimental realization of all-optical non-invasive control by means of time-delayed feed-

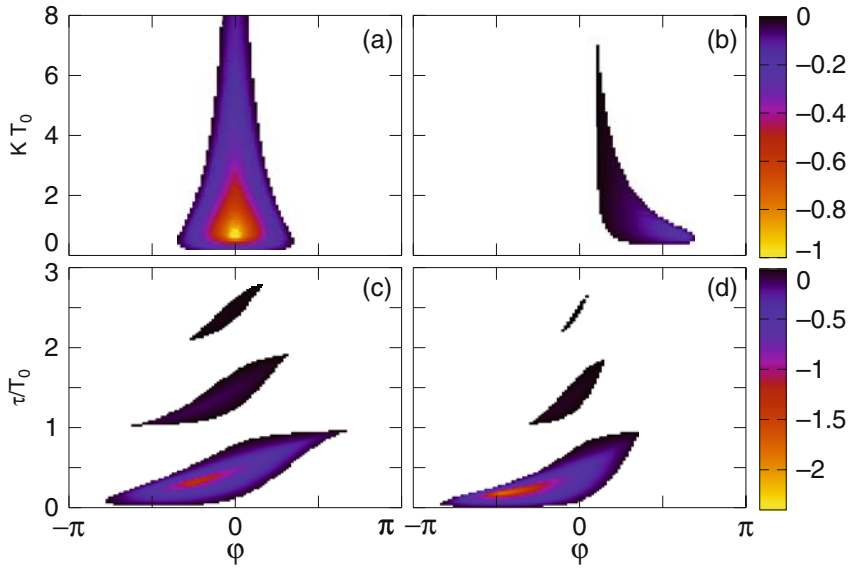

Fig. 4.27 Domain of control in dependence on φ, K, and τ with normalization in units of $T_0 = 2\pi/\omega$. The largest real part of the complex eigenvalues Λ is shown in *colorcode*. (**a**), (**b**): Domain of control in the (φ, K) plane for fixed delay $\tau = T_0/2$ and $0.9T_0$, respectively. (**c**), (**d**): Domain of control in the (φ, τ) plane for fixed feedback gain $K = 1/T_0$ and $2/T_0$, respectively. Fixed parameter: $\lambda = 0.2/T_0$ [38]

back from an external Fabry–Perot cavity [38]. They are also in qualitative agreement with simulations of more realistic laser models of Lang–Kobayashi [144] and traveling-wave type [38, 146].

In conclusion, using phase-dependent feedback, stabilization of the continuous-wave laser output and non-invasive suppression of intensity pulsations has been shown. This study demonstrates the crucial importance of the proper choice of phase of the feedback signal, i.e., of the coupling matrix, which represents a generic feature of all-optical time-delayed feedback control.

4.3.2 Noise Suppression by Time-Delayed Feedback

In this section we investigate the effects of feedback under the influence of noise in a semiconductor laser [95]. A laser with feedback from a conventional mirror can be described by the Lang–Kobayashi equations [147]. Other types of feedback have also been investigated [143, 148]. One particular feedback realizes the delayed feedback control by a Fabry–Perot resonator [38, 139, 144]. A schematic view of this all-optical setup is shown in Fig. 4.28. A fraction of the emitted laser light is coupled into a resonator. The resonator then feeds an interference signal of the actual electric field $E(t)$ and the delayed electric field $E(t-\tau)$ (neglecting multiple reflections) back into the laser.

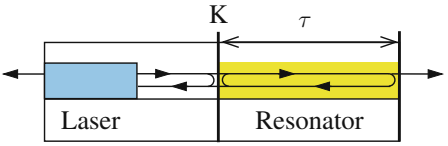

Fig. 4.28 Setup of a laser coupled to a Fabry–Perot resonator realizing the time-delayed feedback control [95]

Scaling (i) time by the photon lifetime $\tau_p \approx 10^{-12}$s, (ii) carrier density (in excess of the threshold carrier density) by the inverse of the differential gain G_N times τ_p, and (iii) electric field by $(\tau_c G_N)^{-1/2}$, where $\tau_c \approx 10^{-9}$s is the carrier lifetime (for details see [149]), one obtains a modified set of non-dimensionalized Lang–Kobayashi equations [139] describing this setup

$$\begin{aligned} \frac{d}{dt}E &= \frac{1}{2}(1+i\,\alpha)\,n\,E \\ &\quad -e^{i\varphi}K\,[E(t)-e^{i\psi}E(t-\tau)]+F_E(t), \\ T\,\frac{d}{dt}n &= p-n-(1+n)\,|E|^2, \end{aligned} \tag{4.100}$$

where E is the complex electric field amplitude, n is the carrier density in excess of the laser threshold, α is the linewidth enhancement factor, K is the feedback strength, τ is the roundtrip time in the Fabry–Perot resonator, p is the excess pump injection current, $T = \tau_c/\tau_p$ is the timescale parameter, F_E is a noise term describing the spontaneous emission, and φ and ϕ are optical phases.

The phases φ and ψ depend on the sub-wavelength positioning of the mirrors. By precise tuning $\varphi = 2\pi n$ and $\psi = 2\pi m$ one can realize the usual Pyragas feedback control

$$-K\,[E(t)-E(t-\tau)]. \tag{4.101}$$

We consider small feedback strength K, so that the laser is not destabilized and no delay-induced bifurcations occur. A sufficient condition [139] is that

$$K < K_c = \frac{1}{\tau\sqrt{1+\alpha^2}}. \tag{4.102}$$

The noise term F_E in (4.100) arises from spontaneous emission, and we assume the noise to be white and Gaussian

$$\langle F_E\rangle = 0, \qquad \langle F_E(t)\,\overline{F_E(t')}\rangle = R_{sp}\delta(t-t'), \tag{4.103}$$

with the spontaneous emission rate

$$R_{sp} = \beta(n+n_0), \tag{4.104}$$

where β is the spontaneous emission factor and n_0 is the threshold carrier density. Without noise the laser operates in a steady state (*cw emission*). To find these steady state values, we transform (4.100) into equations for intensity I and phase ϕ by $E = \sqrt{I}\, e^{i\phi}$:

$$\begin{aligned} \frac{d}{dt} I &= n\, I - 2K\, [I - \sqrt{I}\sqrt{I_\tau}\, \cos(\phi_\tau - \phi)] + R_{sp} + F_I(t), \\ \frac{d}{dt}\phi &= \frac{1}{2}\alpha\, n + K\, \frac{\sqrt{I_\tau}}{\sqrt{I}}\, \sin(\phi_\tau - \phi) + F_\phi(t), \\ T\, \frac{d}{dt} n &= p - n - (1+n)\, I, \end{aligned} \tag{4.105}$$

where $I_\tau = I(t-\tau)$, $\phi_\tau = \phi(t-\tau)$, and

$$\langle F_I \rangle = 0, \quad \langle F_\phi \rangle = 0, \tag{4.106}$$

$$\langle F_I(t)\, F_\phi(t') \rangle = 0, \tag{4.107}$$

$$\langle F_I(t)\, F_I(t') \rangle = 2R_{sp}\, I\, \delta(t-t') \tag{4.108}$$

$$\langle F_\phi(t)\, F_\phi(t') \rangle = \frac{R_{sp}}{2I}\, \delta(t-t'). \tag{4.109}$$

Setting $\frac{d}{dt} I = 0$, $\frac{d}{dt} n = 0$, $\frac{d}{dt}\phi = \text{const}$, and $K = 0$ and replacing the noise terms by their mean values give a set of equations for the mean steady state solutions I_*, n_*, and $\phi = \omega_* t$ without feedback (the solitary laser mode). Our aim is now to analyze the stability (damping rate) of the steady state. A high stability of the steady state, corresponding to a large damping rate, will give rise to small-amplitude noise-induced relaxation oscillations whereas a less stable steady state gives rise to stronger relaxation oscillations. Linearizing (4.105) around the steady state $X(t) = X_* + \delta X(t)$, with $X(t) = (I,\, \phi,\, n)$, gives

$$\frac{d}{dt} X(t) = U\, X(t) - V\, [X(t) - X(t-\tau)] + F(t), \tag{4.110}$$

with

$$U = \begin{bmatrix} n_* & 0 & I_* + \beta \\ 0 & 0 & \frac{1}{2}\alpha \\ -\frac{1}{T}(1+n_*) & 0 & -\frac{1}{T}(1+I_*) \end{bmatrix}, \tag{4.111}$$

(4.112)

$$V = \text{diag}(K,\, K,\, 0), \tag{4.113}$$

where diag(...) denotes a 3×3 diagonal matrix, and

$$F = (F_I,\, F_\phi,\, 0). \tag{4.114}$$

The Fourier transform of (4.110) gives

$$\widehat{X}(\omega) = \underbrace{[i\omega - U + V\,(1 - e^{-i\omega\tau})]^{-1}}_{\equiv M}\,\widehat{F}(\omega). \tag{4.115}$$

The Fourier-transformed covariance matrix of the noise is

$$\langle \widehat{F}(\omega)\,\widehat{F}(\omega')^{\dagger}\rangle = \frac{1}{2\pi}\mathrm{diag}(2R_{sp}I_{*},\,\frac{R_{sp}}{2I_{*}},\,0)\,\delta(\omega-\omega'), \tag{4.116}$$

with the adjoint †. The matrix-valued power spectral density $S(\omega)$ can then be defined through

$$S(\omega)\,\delta(\omega-\omega') = \langle \widehat{X}(\omega)\,\widehat{X}(\omega)^{\dagger}\rangle \tag{4.117}$$

and is thus given by

$$S(\omega) = \frac{1}{2\pi}\,M\,\mathrm{diag}(2R_{sp}I_{*},\,\frac{R_{sp}}{2I_{*}},\,0)\,M^{\dagger}. \tag{4.118}$$

The diagonal elements of the matrix S are the power spectrum of the intensity $S_{\delta I}$, the phase $S_{\delta\phi}$, and the carrier density $S_{\delta n}$. The frequency power spectrum is related to the phase power spectrum $S_{\delta\phi}(\omega)$ by [150]:

$$S_{\delta\dot{\phi}}(\omega) = \omega^{2}\,S_{\delta\phi}(\omega). \tag{4.119}$$

The laser parameters we consider in the following are typical values for a single mode distributed feedback (DFB) laser operating close to threshold [139, 150].

Figures 4.29 and 4.30 display the intensity and the frequency power spectra, respectively, for different values of the delay time τ, obtained analytically from the linearized equations (left) and from simulations of the full nonlinear equations (right). All spectra have a main peak at the relaxation oscillation frequency

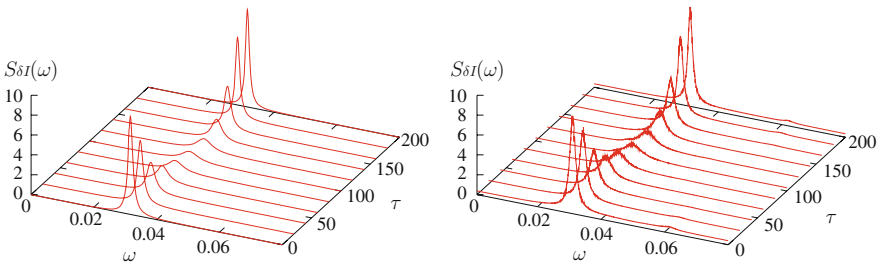

Fig. 4.29 Analytical (*left*) and numerical (*right*) results for the power spectral density $S_{\delta I}(\omega)$ of the intensity for different values of the delay time τ. Parameters: $p = 1$, $T = 1000$, $\alpha = 2$, $\beta = 10^{-5}$, $n_0 = 10$, and $K = 0.002$. (A typical unit of time is the photon lifetime $\tau_p = 10^{-11}$ s, corresponding to a frequency of 100 GHz) [95]

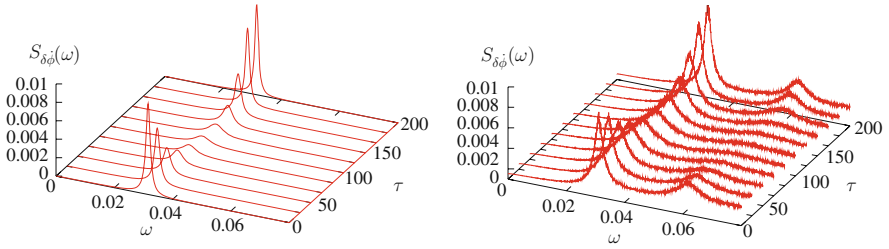

Fig. 4.30 Analytical (*left*) and numerical (*right*) results for the power spectral density $S_{\delta\phi}(\omega)$ of the frequency for different values of the delay time τ. Parameters: $p = 1$, $T = 1000$, $\alpha = 2$, $\beta = 10^{-5}$, $n_0 = 10$, and $K = 0.002$ [95]

$\Omega_{RO} \approx 0.03$. The higher harmonics can also be seen in the spectra obtained from the nonlinear simulations. The main peak decreases with increasing τ and reaches a minimum at

$$\tau_{opt} \approx \frac{T_{RO}}{2} = \frac{2\pi}{2\Omega_{RO}} \approx 100. \tag{4.120}$$

With further increases of τ, the peak height increases again until it reaches approximately its original maximum at $\tau \approx T_{RO}$. A small peak in the power spectra indicates that the relaxation oscillations are strongly damped. This means that the fluctuations around the steady state values I_* and n_* are small. Figure 4.31 displays exemplary time series of the intensity with and without feedback. The time series with feedback shows much less pronounced stochastic fluctuations.

Next, we study the variance of the intensity distribution as a measure for the oscillation amplitude:

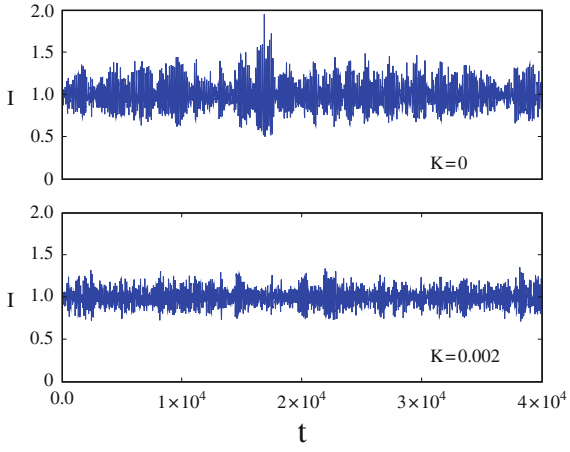

Fig. 4.31 Intensity time series without (*top panel*) and with (*bottom panel*) control. Parameters: $p = 1$, $T = 1000$, $\alpha = 2$, $\beta = 10^{-5}$, $n_0 = 10$, and $\tau = 100 \approx T_0/2$ [95]

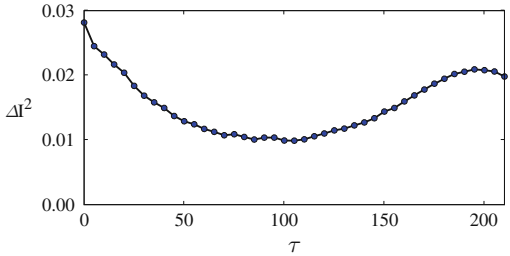

Fig. 4.32 Variance of the intensity I vs. the delay time. Parameters: $p = 1$, $T = 1000$, $\alpha = 2$, $\beta = 10^{-5}$, $n_0 = 10$, and $K = 0.002$ [95]

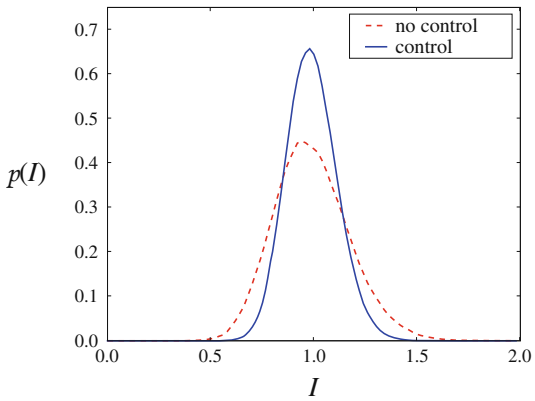

Fig. 4.33 Probability distribution of the intensity I with and without the resonator (simulations). Parameters: $p = 1$, $T = 1000$, $\alpha = 2$, $\beta = 10^{-5}$, $n_0 = 10$, and $K = 0.002$ [95]

$$\Delta I^2 \equiv \left\langle (I - \langle I \rangle)^2 \right\rangle. \tag{4.121}$$

Figure 4.32 displays the variance as a function of the delay time. The variance is minimum at $\tau \approx T_{RO}/2$, thus for this value of τ the intensity is most steady and relaxation oscillations excited by noise have a small amplitude.

Figure 4.33 displays the intensity distribution of the laser without (dashed) and with (solid) optimal control. The time-delayed feedback control leads to a narrower distribution and less fluctuations.

In conclusion, by tuning the cavity roundtrip time of the feedback loop to half the relaxation oscillation period, $\tau_{opt} \approx T_{RO}/2$, noise-induced oscillations in a semiconductor laser can be suppressed to a remarkable degree.

4.4 Time-Delayed Control of Neuronal Dynamics

In this section we study the effect of time-delayed feedback in neural systems [94]. Time delays can occur in the coupling between different neurons due to signal propagation or in a self-feedback loop, e.g., due to neurovascular coupling in the

brain. Moreover, time-delayed feedback loops might be deliberately implemented to control neural disturbances, e.g., to suppress undesired synchrony of firing neurons in Parkinson's disease or epilepsy [71, 72]. Here we model the neurons in the framework of the FitzHugh–Nagumo model [151, 152], which is a simple paradigm of excitable dynamics. Time-delayed feedback control of noise-induced oscillations was demonstrated in a single excitable FitzHugh–Nagumo system [26, 27, 89, 91]. The simplest network configuration displaying features of neural interaction consists of two coupled excitable systems. In two coupled FitzHugh–Nagumo systems two situations are studied: (i) stochastic synchronization of instantaneously coupled neurons under the influence of white noise and controlled by local time-delayed feedback [93, 153] and (ii) the emergence of antiphase oscillations in delay-coupled neurons and complex scenarios induced by the additional application of time-delayed self-feedback such as transitions from synchronized in-phase to antiphase oscillations, bursting patterns, or amplitude death [94, 154]. In spatially extended neuronal media time-delayed feedback as well as nonlocal spatial coupling has also been studied, and it has been shown that pulse propagation in a reaction–diffusion system can be suppressed by appropriate choice of the space or timescales of the feedback [22, 23], which suggests failure of feedback as a common mechanism for spreading depolarization waves in migraine aura and stroke. However, in the present section we restrict ourselves to spatially homogeneous coupled FitzHugh–Nagumo systems.

4.4.1 Model of Two Coupled Neurons

In order to grasp the complicated interaction between billions of neurons in large neural networks, those are often lumped into groups of neural populations each of which can be represented as an effective excitable element that is mutually coupled to the other elements [145, 72]. In this sense the simplest model which may reveal features of interacting neurons consists of two coupled neural oscillators. Each of these will be represented by a simplified FitzHugh–Nagumo system, which is often used as a paradigmatic generic model for neurons, or more generally, excitable systems [34].

Neurons are excitable units that can emit spikes or bursts of electrical signals, i.e., the system rests in a stable steady state, but after it is excited beyond a threshold, it emits a pulse. In the following, we consider electrically coupled neurons (Fig. 4.34 a) modeled by the FitzHugh–Nagumo system in the excitable regime:

$$\begin{aligned}
\epsilon_1 \dot{u}_1 &= u_1 - \frac{u_1^3}{3} - v_1 + C[u_2(t-\tau) - u_1(t)] \\
\dot{v}_1 &= u_1 + a + D_1 \xi_1(t) \\
\epsilon_2 \dot{u}_2 &= u_2 - \frac{u_2^3}{3} - v_2 + C[u_1(t-\tau) - u_2(t)] \\
\dot{v}_2 &= u_2 + a + D_2 \xi_2(t),
\end{aligned} \tag{4.122}$$

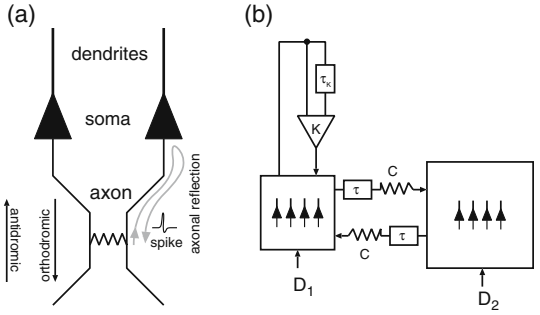

Fig. 4.34 (**a**) Scheme of two axo-axonally coupled neurons (pyramidal cells coupled by an electrical synapse) [155]. (**b**) Two mutually coupled neural populations (delay τ, coupling constant C) with feedback control loop (delay τ_K, coupling constant K) and noise input D_1, D_2 [94]

where the subsystems u_1, v_1 and u_2, v_2 correspond to single neurons (or neuron populations), which are linearly coupled with coupling strength C. The variables u_1 and u_2 are related to the transmembrane voltage and v_1 and v_2 refer to various quantities connected to the electrical conductance of the relevant ion currents. Here a is an excitability parameter whose value defines whether the system is excitable ($a > 1$) or exhibits self-sustained periodic firing ($a < 1$), ϵ_1 and ϵ_2 are the timescale parameters that are usually chosen to be much smaller than unity, corresponding to fast activator variables u_1, u_2 and slow inhibitor variables v_1, v_2.

The synaptic coupling between two neurons is modeled as a diffusive coupling considered for simplicity to be symmetric [156–158]. More general delayed couplings are considered in [159]. The coupling strength C summarizes how information is distributed between neurons. The mutual delay τ in the coupling is motivated by the propagation delay of action potentials between the two neurons u_1 and u_2. Time delays in the coupling must be considered particularly in the case of high-frequency oscillations.

Each neuron is driven by Gaussian white noise $\xi_i(t)$ ($i = 1, 2$) with zero mean and unity variance. The noise intensities are denoted by parameters D_1 and D_2.

Besides the delayed coupling we will also consider delayed self-feedback in the form suggested by Pyragas [6], where the difference $s(t) - s(t - \tau_K)$ of a system variable s (e.g., activator or inhibitor) at time t and at a delayed time $t - \tau_K$, multiplied by some control amplitude K, is coupled back into the same system (Fig. 4.34b). Such feedback loops might arise naturally in neural systems, e.g., due to neurovascular coupling that has a characteristic latency or due to finite propagation speed along cyclic connections within a neuron sub-population or they could be realized by external feedback loops as part of a therapeutical measure, as proposed in [72]. This feedback scheme is simple to implement, quite robust, and has already been applied successfully in a real experiment with time-delayed neurofeedback from real-time magnetoencephalography (MEG) signals to humans via visual stimulation in order to suppress the alpha rhythm, which is observed due to strongly synchronized neural populations in the visual cortex in the brain [160]. One distinct advantage of this

method is its non-invasiveness, i.e., in the ideal deterministic limit the control force vanishes on the target orbit, which may be a steady state or a periodic oscillation of period τ. In the case of noisy dynamics the control force, of course, does not vanish but still remains small, compared to other common control techniques using external periodic signals, for instance, in deep brain stimulation to suppress neural synchrony in Parkinson's disease [161].

The phase portrait and the nullclines of a single FitzHugh–Nagumo system without noise and feedback are shown in Fig. 4.35(a). The fixed point A is a stable focus or node for $a > 1$ (*excitable regime*). If the system is perturbed well beyond point A' (see inset), it performs a large excursion $A \to B \to C \to D \to A$ in phase space corresponding to the emission of a spike (Fig. 4.35b). At $a = 1$ the system exhibits a Hopf bifurcation of a limit cycle, and the fixed point A becomes an unstable focus for $a < 1$ (*oscillatory regime*).

In the following we choose the excitability parameter $a = 1.05$ in the excitable regime close to threshold. If noise is present, it will occasionally kick the system beyond A' resulting in noise-induced oscillations (*spiking*).

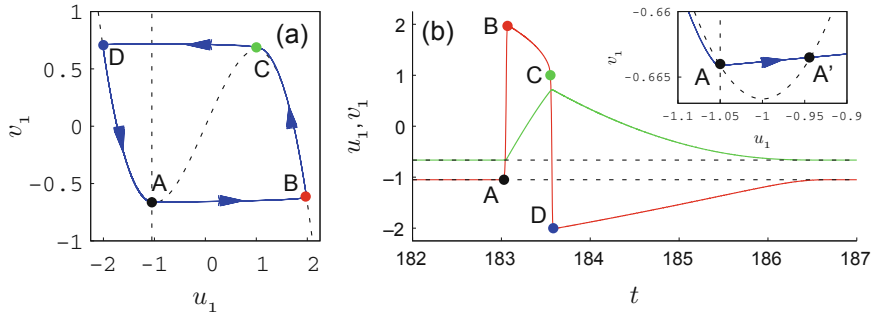

Fig. 4.35 Excitable dynamics of a single FitzHugh–Nagumo system: (**a**) phase portrait (u_1, v_1) (trajectory: *solid blue* and nullclines: *dashed black*), (**b**) time series of activator $u_1(t)$ (*red*) and inhibitor $v_1(t)$ (*green*). The colored dots A, B, C, and D mark corresponding points on panels (**a**) and (**b**). The inset in (**b**) shows a blowup of the phase portrait near A. Parameters: $\epsilon_1 = 0.01$, $a = 1.05$, and $D_1 = 0$ [94]

4.4.2 Control of Stochastic Synchronization

We shall first consider two coupled FitzHugh–Nagumo systems as in (4.122) albeit without delay in the coupling ($\tau = 0$). Noise can induce oscillations even though the fixed point is stable. The noise sources then play the role of stimulating the excitable subsystems. Even if only one subsystem is driven by noise, it induces oscillations of the whole system through the coupling. In this subsection, we consider two non-identical neurons, described by different timescales $\epsilon_1 = 0.005$ and $\epsilon_2 = 0.1$, and set the noise intensity D_2 in the second subsystem equal to a small value, $D_2 = 0.09$, in order to model some background noise level. Depending on the coupling strength

C and the noise intensity D_1 in the first subsystem, the two neurons show weak, moderate, or strong stochastic synchronization [93].

If feedback is applied to one of the two interacting subsystems [93, 153], i.e., locally, the dynamical equations are given by:

$$\begin{aligned} \epsilon_1 \dot{u}_1 &= u_1 - \frac{u_1^3}{3} - v_1 + C\,(u_2 - u_1)\,, \\ \dot{v}_1 &= u_1 + a + K\,[v_1(t-\tau) - v_1(t)] + D_1\,\xi(t), \end{aligned} \tag{4.123}$$

$$\begin{aligned} \epsilon_2 \dot{u}_2 &= u_2 - \frac{u_2^3}{3} - v_2 + C\,(u_1 - u_2)\,, \\ \dot{v}_2 &= u_2 + a + D_2\,\xi_2(t), \end{aligned} \tag{4.124}$$

where subsystems (4.123) and (4.124) represent two different neurons, and local feedback with strength K and delay time τ is applied to the first subsystem.

There are various measures of the synchronization of coupled systems [162]. For instance, one can consider the average interspike intervals (ISI) of each subsystem, i.e., $\langle T_1 \rangle$ and $\langle T_2 \rangle$, calculated from the u variable of the respective subsystem. Their ratio $\langle T_1 \rangle / \langle T_2 \rangle$ is a measure of frequency synchronization. Other measures for stochastic synchronization are given by the phase synchronization index [93] or the mean phase synchronization intervals [153].

First, we consider subsystems (4.123) and (4.124) with $D_1 = 0.6$ and $C = 0.2$, which corresponds to a moderately synchronized uncontrolled system. We aim to find out if the feedback can make the subsystems more, or less, synchronous, and their global dynamics more or less coherent. In particular, we are interested if perfect 1:1 synchronization can be induced by the local feedback or if the existing synchronization can be destroyed. The ratio of ISIs and the synchronization index $\gamma_{1,1}$ are shown by color code in Fig. 4.36 for a large range of the values of the feedback delay τ and strength K. The lighter areas are associated with the stronger 1:1 synchronization, and the values at $K = 0$ and at $\tau = 0$ characterize the original state of the system without feedback. As seen from Fig. 4.36, the locally applied delayed feedback is able to move the system's state closer to the 1:1 synchronization with suitable feedback parameters. On the other hand, for $\tau \approx 2.5$ (black area), 1:1 synchronization is suppressed.

Next, we consider weakly synchronized subsystems (4.123) and (4.124) that are further from the 1:1 synchronization region under the influence of the controlling feedback. For $D_1 = 0.6$ and $C = 0.1$, the ratio of ISIs and the synchronization index $\gamma_{1,1}$ are shown by color code in Fig. 4.37. Again, the stochastic synchronization can be strongly modulated by changing the delay time, i.e., one can either enhance or suppress synchronization by appropriate choice of the local feedback delay.

Finally, for the system that is very well synchronized from the beginning at $D_1 = 0.15$ and $C = 0.2$ again delayed feedback can either enhance or suppress synchronization (Fig. 4.38). In view of applications, where neural synchronization is often pathological, e.g., in Parkinson's disease or epilepsy, it is interesting to note

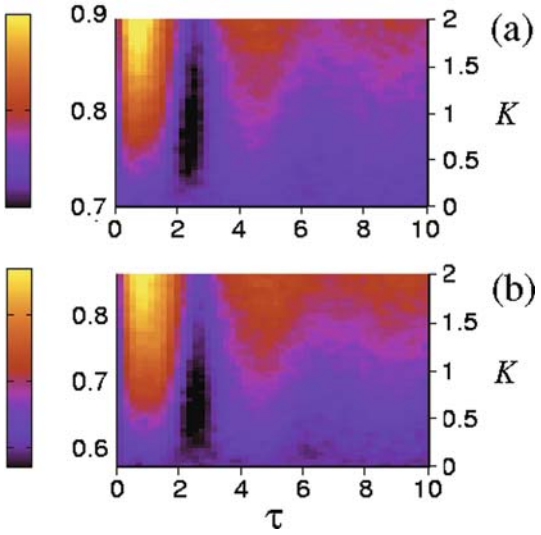

Fig. 4.36 Effect of delayed feedback on frequency and phase synchronizations between the two subsystems at $D_1 = 0.6$ and $C = 0.2$ (moderate synchronization). (**a**) Ratio of average interspike intervals $\langle T_1 \rangle / \langle T_2 \rangle$ from the two systems and (**b**) synchronization index $\gamma_{1,1}$ vs. the control strength K and the time delay τ [93]

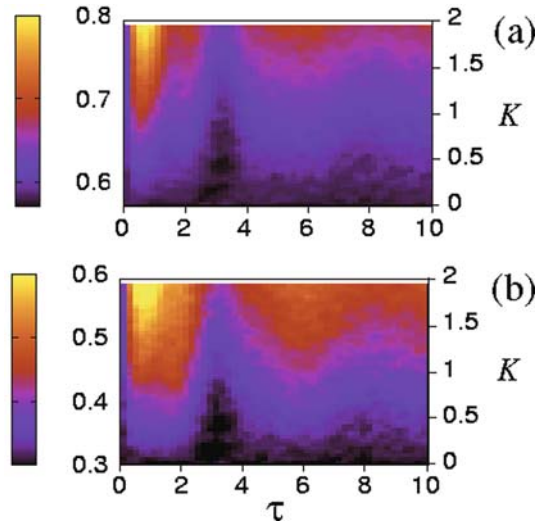

Fig. 4.37 Same as Fig. 4.36 for $D_1 = 0.6$ and $C = 0.1$ (weak synchronization) [93]

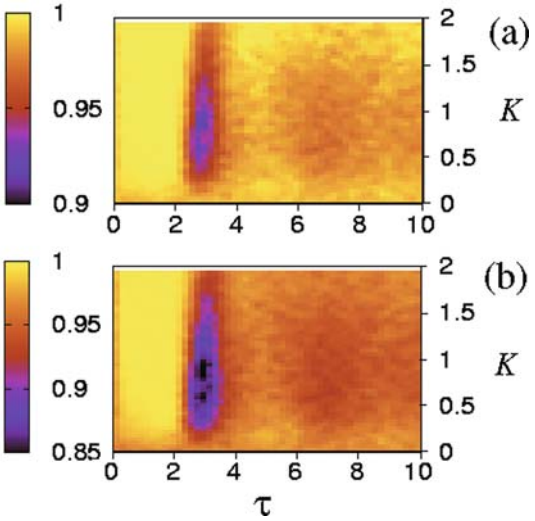

Fig. 4.38 Same as Fig. 4.36 for $D_1 = 0.15$ and $C = 0.2$ (strong synchronization) [93]

that there are cases where a proper choice of the local feedback control parameters leads to desynchronization of the coupled system (dark regions in all three figures).

4.4.3 Dynamics of Delay-Coupled Neurons

In this section we study the influence of a delay in the coupling of two neurons [94, 154], rather than a delayed self-feedback ($K = 0$). We set the noise terms in (4.122) equal to zero, $D_1 = D_2 = 0$, but consider a time delay τ in the coupling. In the deterministic system the delayed coupling plays the role of a stimulus which can induce self-sustained oscillations in the coupled system even if the fixed point is stable. In this sense the delayed coupling has a similar effect as the noise term in the previous section. Here the bifurcation parameters for delay-induced bifurcations are the coupling parameters C and τ.

In the following we shall choose symmetric timescales $\epsilon_1 = \epsilon_2 = \epsilon = 0.01$ and fix $a = 1.05$, where each of the two subsystems has a stable fixed point and exhibits excitability.

The unique fixed point of the system is symmetric and is given by $\mathbf{u}^* \equiv (u_1^*, v_1^*, u_2^*, v_2^*)$, where $u_i^* = -a$ and $v_i^* = a^3/3 - a$. Linearizing (4.122) around the fixed point $\mathbf{u}^*$ by setting $\mathbf{u}(t) = \mathbf{u}^* + \delta\mathbf{u}(t)$, one obtains:

$$\delta\dot{\mathbf{u}} = \frac{1}{\epsilon}\begin{pmatrix} \xi & -1 & 0 & 0 \\ \epsilon & 0 & 0 & 0 \\ 0 & 0 & \xi & -1 \\ 0 & 0 & \epsilon & 0 \end{pmatrix} \delta\mathbf{u}(t) + \frac{1}{\epsilon}\begin{pmatrix} 0 & 0 & C & 0 \\ 0 & 0 & 0 & 0 \\ C & 0 & 0 & 0 \\ 0 & 0 & 0 & 0 \end{pmatrix} \delta\mathbf{u}(t-\tau), \qquad (4.125)$$

where $\xi = 1 - a^2 - C$. The ansatz

$$\delta\mathbf{u}(t) = e^{\lambda t}\mathbf{u}, \tag{4.126}$$

where $\mathbf{u}$ is an eigenvector of the Jacobian matrix, leads to the characteristic equation for the eigenvalues λ:

$$(1 - \xi\lambda + \epsilon\lambda^2)^2 - (\lambda C e^{-\lambda\tau})^2 = 0, \tag{4.127}$$

which can be factorized giving

$$1 - \xi\lambda + \epsilon\lambda^2 \pm \lambda C e^{-\lambda\tau} = 0. \tag{4.128}$$

This transcendental equation has infinitely many complex solutions λ. The real parts of all eigenvalues are negative throughout, i.e., the fixed point of the coupled system remains stable for all C. This can be shown analytically for $a > 1$ by demonstrating that no delay-induced Hopf bifurcation can occur. Substituting the ansatz $\lambda = i\omega$ into (4.128) and separating into real and imaginary parts yields for the imaginary part

$$\xi = \pm C\cos(\omega\tau). \tag{4.129}$$

This equation has no solution for $a > 1$ since $|\xi| = a^2 - 1 + C > C$, which proves that a Hopf bifurcation cannot occur.

Delay-induced oscillations in excitable systems are inherently different from noise-induced oscillations. The noise term continuously kicks the subsystems out of their respective rest states and thus induces sustained oscillations. Instantaneous coupling without delay then produces synchronization effects between the individual oscillators [93, 153]. For *delayed* coupling the case is entirely different. Here the impulse of one neuron triggers the other neuron to emit a spike, which in turn, after some delay, triggers the first neuron to emit a spike. Hence self-sustained periodic oscillations can be induced without the presence of noise (Fig. 4.39). It is evident that the oscillations of the two neurons have a phase lag of π. The period of the oscillations is given by $T = 2(\tau + \delta)$ with a small quantity $\delta > 0$.

In order to understand this additional phase shift δ, we shall now consider in detail the different stages of the oscillation as marked in Fig. 4.35. Due to the small value of $\epsilon \ll 1$ there is a distinct timescale separation between the fast activators and the slow inhibitors, and a single FitzHugh–Nagumo system performs a fast horizontal transition $A \to B$, then travels slowly approximately along the right stable branch of the u_1 nullcline $B \to C$ (*firing*), then jumps back fast to D, and returns slowly to the *rest state* A approximately along the left stable branch of the u_1 nullcline (*refractory phase*). If a is close to unity, these four points are approximately given by $A = (-a, -a + \frac{a_1^3}{3})$, $B = (2, -\frac{2}{3})$, $C = (1, \frac{2}{3})$, and $D = (-2, \frac{2}{3})$. A rough estimate for A' is $(a - 2, -a + \frac{a_1^3}{3})$. The two slow phases $B \to C$ and $D \to A$ can be approximated by $v_1 \approx u_1 - \frac{u_1^3}{3}$ and hence $\dot{v}_1 \approx \dot{u}_1(1 - u_1^2) = u_1 + a$ which gives

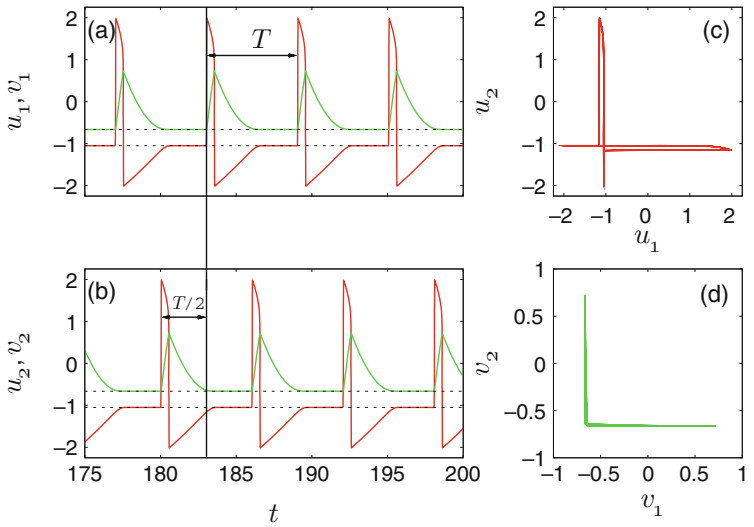

Fig. 4.39 Delay-induced oscillations. (**a**), (**b**): Time series of both subsystems (*red solid lines*: activator u_i, *green solid lines*: inhibitor v_i, and *black dashed lines*: fixed point values of activator and inhibitor). (**c**), (**d**): Phase portraits of activators (**c**) and inhibitors (**d**). Parameters: $a = 1.05$, $\epsilon = 0.01$, $C = 0.5$, and $\tau = 3$ [94]

$$\dot{u}_1 = \frac{u_1 + a}{1 - u_1^2}, \tag{4.130}$$

which can be solved analytically, describing the firing phase (+) and the refractory phase (−):

$$\int_{\pm 2}^{u} dx_1 \frac{1 - u_1^2}{u_1 + a} = (a^2 - 1) \ln \frac{a \pm 2}{a + u} - a(\pm 2 - u) + 2 - \frac{u^2}{2} = t. \tag{4.131}$$

Integrating from B to C gives the firing time

$$T_f = \int_2^1 dx_1 \frac{1 - u_1^2}{u_1 + a} = (a^2 - 1) \ln \frac{a + 2}{a + 1} - a + \frac{3}{2}. \tag{4.132}$$

For $\epsilon = 0.01$, $a = 1.05$ the analytical solution is in good agreement with the numerical solution in Fig. 4.35(b), including the firing time $T_f = 0.482$ (analytical approximation: 0.491).

For a rough estimate, in the following we shall approximate the spike by a rectangular pulse

$$u_1(t) \approx \begin{cases} 2 & \text{if } t < T_f, \\ -a & \text{if } t \geq T_f. \end{cases} \tag{4.133}$$

If the first subsystem is in the rest state, and a spike of the second subsystem arrives at $t = 0$ (after the propagation delay τ), we can approximate the initial dynamic response by linearizing u_1, v_1 around the fixed point (u_1^*, v_1^*) and approximating the feedback by a constant impulse during the firing time T_f. The fast dynamic response along the u_1 direction is then given by

$$\epsilon \delta \dot{u}_1 = \xi \delta u_1 + 2C \tag{4.134}$$

with $\xi < 0$. This inhomogeneous linear differential equation can be solved with the initial condition $u_1(0) = -a$:

$$u_1(t) = -a + \frac{2C}{|\xi|}(1 - e^{-\frac{|\xi|}{\epsilon}t}). \tag{4.135}$$

Note that this equation is not valid for large t since (i) the linearization breaks down, and (ii) the pulse duration T_f is exceeded. For small t (4.135) can be expanded as

$$u_1(t) = -a + \frac{2C}{\epsilon}t, \tag{4.136}$$

which is equivalent to neglecting the upstream flow field $-|\xi|\delta u_1$ in (4.134) near the stable fixed point A compared to the pulling force $2C$ of the remote spike which tries to excite the system toward B. Once the system has crossed the middle branch of the u_1 nullcline at A', the intrinsic flow field accelerates the trajectory fast toward B, initiating the firing state. Therefore there is a turn-on delay δ, given by the time the trajectory takes from A to A', i.e., $u_1(\delta) \approx a - 2$, according to (4.136):

$$\delta = (a - 1)\frac{\epsilon}{C}. \tag{4.137}$$

Since the finite rise time of the impulse has been neglected in our estimate, the exact solution δ is slightly larger and does not vanish at $a = 1$.

With increasing a the distance A–A' increases and so does δ. The small additional phase shift δ between the spike $u_1(t)$ and the delayed pulse $u_2(t - \tau)$ results in a non-vanishing coupling term at the beginning and at the end of the spike $u_1(t)$. It is the reason (i) that the spike is initiated and (ii) that it is terminated slightly before the turning point of the u_1 nullcline. The latter effect becomes more pronounced if a is increased or τ is decreased (Fig. 4.40). Both lead to a shift of the initial starting point of the spike emission on the left branch of the nullcline toward D, and hence to a longer distance up to the middle branch of the nullcline which has to be overcome by the impulse u_2, hence to a larger turn-on delay δ, and therefore to an earlier termination of the spike u_1. This explains that the firing phase is shortened, and the limit cycle loop is narrowed from both sides with increasing a or decreasing τ, see Fig. 4.40. In the case of $a = 1.05$ and $\tau = 3$ (Fig. 4.40 a), the delay time is large enough for the two subsystems to nearly approach the fixed point A before being perturbed again by the remote signal. If the delay time becomes much smaller, e. g., for $\tau = 0.8$ (Fig. 4.40 b), the excitatory spike of the other subsystem arrives while

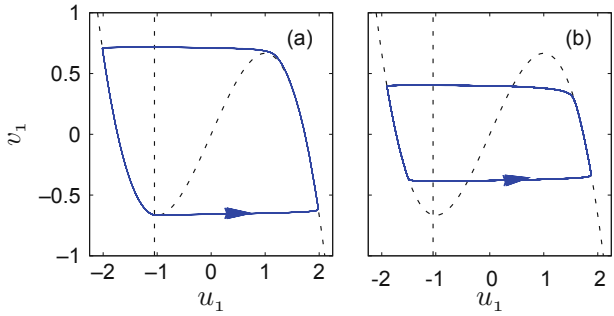

Fig. 4.40 Phase portraits of delay-coupled excitable system (u_1, v_1) for different delay times τ (trajectories: *solid blue* and nullclines: *dashed black*). (**a**) $\tau = 3$ ($\delta = 0.009$) and (**b**) $\tau = 0.8$ ($\delta = 0.015$). Other parameters: $a = 1.05$, $\epsilon = 0.01$, and $C = 0.5$ [94]

the first system is still in the refractory phase, so that it cannot complete the return $D \to A$ to the fixed point. In this case, a in (4.137) has to be substituted by a larger value $\tilde{a}$ with $a < \tilde{a} < 1.7$ in order to get a better estimate of δ. Note that without the phase shift δ the coupling term $C[u_2(t-\tau) - u_1(t)]$ would always vanish in the 2τ periodic state.

Next, we shall investigate conditions upon the coupling parameters C and τ allowing for limit cycle oscillations. On one hand, if τ becomes smaller than some $\tau_{\min}$, the impulse from the excitatory neuron arrives too early to trigger a spike, since the system is still early in its refractory phase. On the other hand, if C becomes too small, the coupling force of the excitatory neuron is too weak to excite the system above its threshold and pull it far enough toward B.

In Fig. 4.41 the regime of oscillations is shown in the parameter plane of the coupling strength C and coupling delay τ. The oscillation period is color coded. The boundary of this colored region is given by the minimum coupling delay $\tau_{\min}$ as a function of C. For large coupling strength, $\tau_{\min}$ is almost independent of C, with decreasing C it sharply increases, and at some small minimum C no oscillations exist at all. At the boundary, the oscillation sets in with finite frequency and amplitude as can be seen in the insets of Fig. 4.41 which show a cut of the parameter plane at $C = 0.8$. The oscillation period increases linearly with τ. The mechanism that generates the oscillation is a saddle-node bifurcation of limit cycles (see inset (b) of Fig. 4.41), creating a pair of a stable and an unstable limit cycle. The unstable limit cycle separates the two attractor basins of the stable limit cycle and the stable fixed point.

4.4.4 Delayed Self-Feedback and Delayed Coupling

In this section we consider the simultaneous action of delayed coupling and delayed self-feedback [94]. Here we choose to apply the self-feedback term symmetrically to both activator equations, but other feedback schemes are also possible:

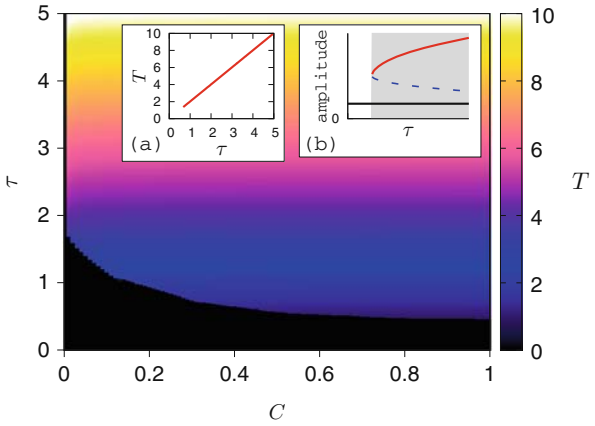

Fig. 4.41 Regime of oscillations in the (τ, C) parameter plane for initial conditions corresponding to single-pulse excitation in one system. The oscillation period T is color coded. The transition between *black* and *color* marks the bifurcation line. Inset (**a**) shows the oscillation period vs. τ in a cut at $C = 0.8$. Inset (**b**): Schematic plot of the saddle-node bifurcation of a stable (*red solid line*) and unstable (*blue dashed*) limit cycle. The maximum oscillation amplitude is plotted vs. the delay time τ and the stable fixed point is plotted as a *solid black line*. The *gray background* marks the bistable region. Parameters: $a = 1.05$, and $\epsilon = 0.01$ [94]

$$\begin{aligned}
\epsilon_1 \dot{u}_1 &= u_1 - \frac{u_1^3}{3} - v_1 + C[u_2(t-\tau) - u_1(t)] + K[u_1(t-\tau_K) - u_1(t)] \\
\dot{v}_1 &= u_1 + a \\
\epsilon_2 \dot{u}_2 &= u_2 - \frac{u_2^3}{3} - v_2 + C[u_1(t-\tau) - u_2(t)] + K[u_2(t-\tau_K) - u_2(t)] \\
\dot{v}_2 &= u_2 + a. \qquad (4.138)
\end{aligned}$$

By a linear stability analysis similar to Sect. 4.4.3 it can be shown that the fixed point remains stable for all values of K and τ_K in the case of $a > 1$, as without self-feedback. Redefining $\xi = 1 - a^2 - C - K$, one obtains the factorized characteristic equation

$$1 - \xi\lambda + \epsilon\lambda^2 = \lambda K e^{-\lambda\tau_K} \pm \lambda C e^{-\lambda\tau} \qquad (4.139)$$

Substituting the Hopf condition $\lambda = i\omega$ and separating into real and imaginary parts yields for the imaginary part

$$-\xi = K\cos(\omega\tau_K) \pm C\cos(\omega\tau) \qquad (4.140)$$

This equation has no solution for $a > 1$ since $|\xi| = a^2 - 1 + C + K > C + K$.

The adopted form of control allows for the synchronization of the two cells not only for identical values of τ and τ_K but also generates an intricate pattern of synchronization islands or stripes in the control parameter plane (Fig. 4.42) corresponding to single-spike in-phase and antiphase oscillations with constant

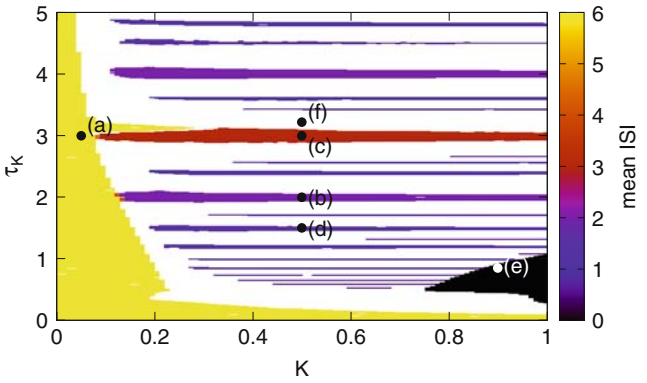

Fig. 4.42 Influence of delayed self-feedback upon coupled oscillations. The mean interspike interval (ISI) is color coded in the control parameter plane of the self-feedback gain K and delay τ_K. *White* areas mark regimes of irregular oscillations where the ISI variance becomes large (> 0.01). Time series corresponding to points (a)–(f) are shown in Fig. 4.43. Other parameters: $a = 1.3$, $\epsilon = 0.01$, $C = 0.5$, and $\tau = 3$ [94]

interspike intervals, see also Fig. 4.43(a–d). Further, for adequately chosen parameter sets of coupling and self-feedback control, we observe effects such as bursting patterns (Fig. 4.43f) and oscillator death (Fig. 4.43e). In addition to these effects, there exists a control parameter regime in which the self-feedback has no effect on the oscillation periods (shaded yellow).

Figure 4.42 shows the control parameter plane for coupling parameters of the uncontrolled system in the oscillatory regime ($C = 0.5$ and $\tau = 3$). We observe three principal regimes: (i) control has no effect on the oscillation period (yellow), although the form of the stable limit cycle is slightly altered (Fig. 4.43a); (ii) islands of in-phase and antiphase synchronization (color coded, see Fig. 4.43 (b–d)); and (iii) oscillator death (black) Fig. 4.43 e).

Figure 4.44 shows the average phase synchronization time as a function of the coupling delay τ and self-feedback delay τ_K for fixed $K = 0.5$. The bright straight rays at rational τ_K/τ indicate long intervals during which both subsystems remain synchronized. A particularly long average synchronization time is found if the two delay times are equal.

In conclusion, we have shown that delayed feedback from other neurons or self-feedback from the same neuron can crucially affect the dynamics of coupled neurons. In the case of noise-induced oscillations in instantaneously coupled neural systems, time-delayed self-feedback can enhance or suppress stochastic synchronization, depending upon the delay time. In the case of delay-coupled neurons without driving noise sources, the propagation delay of the spikes fed back from other neurons can induce periodic antiphase oscillations for sufficiently large coupling strength and delay times. If self-feedback is applied additionally, synchronous zero-lag oscillations can be induced in some ranges of the control parameters, while in other regimes antiphase oscillations or oscillator death as well as more complex bursting patterns can be generated.

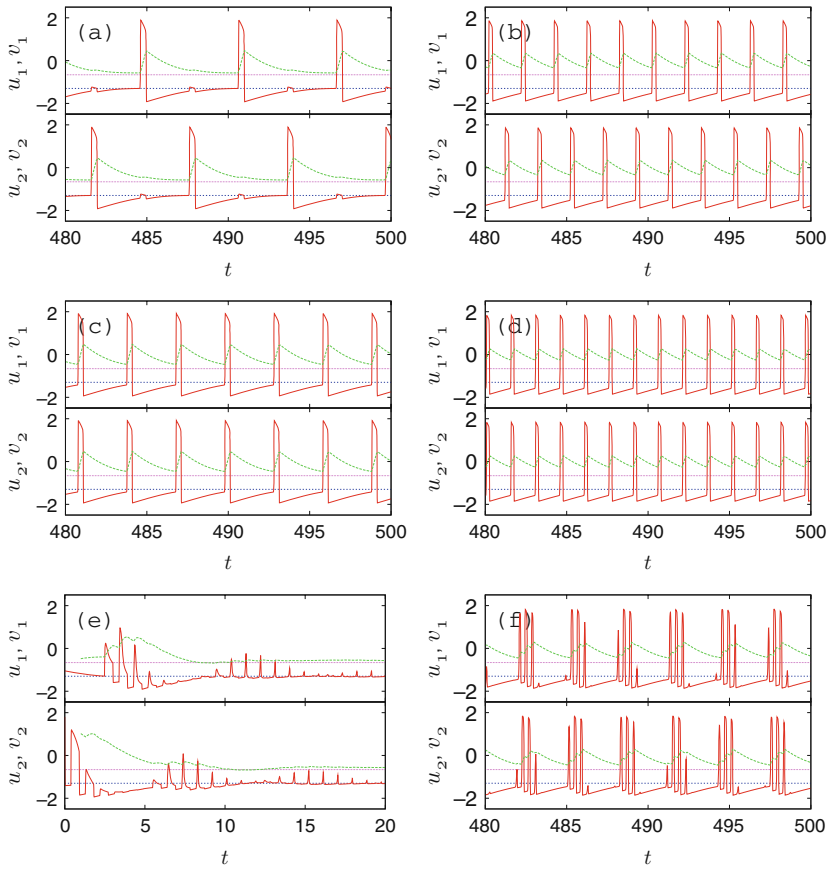

Fig. 4.43 Different modes of oscillation corresponding to different self-feedback parameters K, τ (*red solid lines*: activators $u_i(t)$ and *green solid lines*: inhibitors $v_i(t)$). (**a**), (**b**): Antiphase oscillations for (**a**) $K = 0.05, \tau_K = 3$ (period $T = 6$) and (**b**) $K = 0.5, \tau_K = 2$ ($T = 2$); (**c**), (**d**): in-phase oscillations for (**c**) $K = 0.5, \tau_K = 3$ (period $T = 3$) and (**d**) $K = 0.5, \tau_K = 1.5$ ($T = 1.5$); (**e**): oscillator death for $K = 0.9, \tau_K = 0.9$; and (**f**): bursting pattern for $K = 0.5, \tau_K = 3.2$. Other parameters: $a = 1.3$, $\epsilon = 0.01$, $C = 0.5$, and $\tau = 3$ [94]

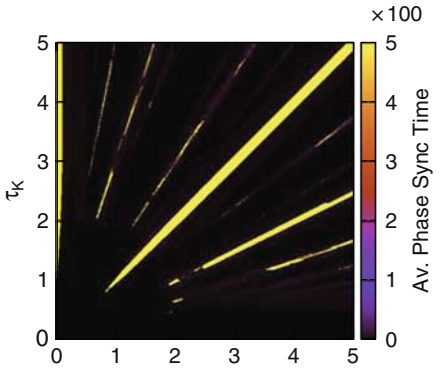

Fig. 4.44 Average phase synchronization time (*color coded*) in the control parameter plane of coupling delay τ and self-feedback delay τ_K. Other parameters: $a = 1.3$, $\epsilon = 0.01$, $C = 0.5$, and $K = 0.5$ [94]

Acknowledgments This work was supported by DFG in the framework of Sfb 555. We are indebted to stimulating collaboration and discussion with A. Amann, A. Balanov, K. Blyuss, S. Brandstetter, T. Dahms, B. Fiedler, D. Gauthier, M. Georgi, B. Hauschildt, F. Henneberger, G. Hiller, N. Janson, W. Just, Y. Kyrychko, A. Panchuk, H. Rittmann-Frank, S. Schiff, S. Schikora, F. Schneider, J. E. S. Socolar, V.Z. Tronciu, M. Wolfrum, H. J. Wünsche, and S. Yanchuk.

References

1. E. Schöll and H. G. Schuster (Eds). *Handbook of Chaos Control*. Wiley-VCH, Weinheim, 2008, second completely revised and enlarged edition.
2. H. Nijmeijer and A. V. D. Schaft. *Nonlinear Dynamical Control Systems*. 3rd ed Springer, New York, 1996.
3. K. Ogata. *Modern Control Engineering*. Prentice-Hall, New York, 1997.
4. A. L. Fradkov, I. V. Miroshnik, and V. O. Nikiforov. *Nonlinear and Adaptive Control of Complex Systems*. Kluwer, Dordrecht, 1999.
5. E. Ott, C. Grebogi, and J. A. Yorke. Controlling chaos. *Phys. Rev. Lett.*, 64, 1196, 1990.
6. K. Pyragas. Continuous control of chaos by self-controlling feedback. *Phys. Lett. A*, 170, 421, 1992.
7. D. J. Gauthier. Resource letter: Controlling chaos. *Am. J. Phys.*, 71, 750, 2003.
8. K. Pyragas. Delayed feedback control of chaos. *Phil. Trans. R. Soc. A*, 364, 2309, 2006.
9. G. Franceschini, S. Bose, and E. Schöll. Control of chaotic spatiotemporal spiking by time-delay autosynchronisation. *Phys. Rev. E*, 60, 5426, 1999.
10. M. Kim, M. Bertram, M. Pollmann, A. von Oertzen, A. S. Mikhailov, H. H. Rotermund, and G. Ertl. Controlling chemical turbulence by global delayed feedback: Pattern formation in catalytic CO oxidation on Pt(110). *Science*, 292, 1357, 2001.
11. O. Beck, A. Amann, E. Schöll, J. E. S. Socolar, and W. Just. Comparison of time-delayed feedback schemes for spatio-temporal control of chaos in a reaction-diffusion system with global coupling. *Phys. Rev. E*, 66, 016213, 2002.
12. N. Baba, A. Amann, E. Schöll, and W. Just. Giant improvement of time-delayed feedback control by spatio-temporal filtering. *Phys. Rev. Lett.*, 89, 074101, 2002.
13. J. Unkelbach, A. Amann, W. Just, and E. Schöll. Time–delay autosynchronization of the spatiotemporal dynamics in resonant tunneling diodes. *Phys. Rev. E*, 68, 026204, 2003.
14. J. Schlesner, A. Amann, N. B. Janson, W. Just, and E. Schöll. Self-stabilization of high frequency oscillations in semiconductor superlattices by time–delay autosynchronization. *Phys. Rev. E*, 68, 066208, 2003.
15. C. Beta, M. Bertram, A. S. Mikhailov, H. H. Rotermund, and G. Ertl. Controlling turbulence in a surface chemical reaction by time-delay autosynchronization. *Phys. Rev. E*, 67, 046224, 2003.
16. C. Beta and A. S. Mikhailov. Controlling spatiotemporal chaos in oscillatory reaction-diffusion systems by time-delay autosynchronization. *Physica D*, 199, 173, 2004.
17. K. A. Montgomery and M. Silber. Feedback control of travelling wave solutions of the complex Ginzburg-Landau equation. *Nonlinearity*, 17, 2225, 2004.
18. E. Schöll, J. Hizanidis, P. Hövel, and G. Stegemann. Pattern formation in semiconductors under the influence of time-delayed feedback control and noise. In: L. Schimansky-Geier, B. Fiedler, J. Kurths, and E. Schöll (eds.), *Analysis and control of complex nonlinear processes in physics, chemistry and biology.* World Scientific, Singapore, 2007, pp. 135–183.
19. C. M. Postlethwaite and M. Silber. Stabilizing unstable periodic orbits in the lorenz equations using time-delayed feedback control. *Phys. Rev. E*, 76, 056214, 2007.
20. A. Ahlborn and U. Parlitz. Controlling spatiotemporal chaos using multiple delays. *Phys. Rev. E*, 75, 65202, 2007.

21. A. Ahlborn and U. Parlitz. Control and synchronization of spatiotemporal chaos. *Phys. Rev. E*, 77, 016201, 2008.
22. M. A. Dahlem, F. M. Schneider, and E. Schöll. Failure of feedback as a putative common mechanism of spreading depolarizations in migraine and stroke. *Chaos*, 18, 026110, 2008.
23. F. M. Schneider, E. Schöll, and M. A. Dahlem. Controlling the onset of traveling pulses in excitable media by nonlocal spatial coupling and time delayed feedback. *Chaos*, 19, 015110, 2009.
24. M. Kehrt, P. Hövel, V. Flunkert, M. A. Dahlem, P. Rodin, and E. Schöll. Stabilization of complex spatio-temporal dynamics near a subcritical Hopf bifurcation by time-delayed feedback. *Eur. Phys. J. B*, 68, 557, 2009.
25. Y. N. Kyrychko, K. B. Blyuss, S. J. Hogan, and E. Schöll. Control of spatio-temporal patterns in the Gray-Scott model. *Chaos* 19, 043126, 2009.
26. N. B. Janson, A. G. Balanov, and E. Schöll. Delayed feedback as a means of control of noise-induced motion. *Phys. Rev. Lett.* 93, 010601, 2004.
27. A. G. Balanov, N. B. Janson, and E. Schöll. Control of noise-induced oscillations by delayed feedback. *Physica D*, 199, 1, 2004.
28. J. Pomplun, A. Amann, and E. Schöll. Mean field approximation of time-delayed feedback control of noise-induced oscillations in the Van der Pol system. *Europhys. Lett.*, 71, 366, 2005.
29. N. B. Janson, A. G. Balanov, and E. Schöll. Control of noise-induced dynamics. In: E. Schöll and H. G. Schuster (eds.), *Handbook of Chaos Control*. Wiley-VCH, Weinheim, 2008, chap. 11, pp. 223–274, second completely revised and enlarged edition.
30. G. Hu, T. Ditzinger, C. Z. Ning, and H. Haken. Stochastic resonance without external periodic force. *Phys. Rev. Lett.*, 71, 807, 1993.
31. A. Pikovsky and J. Kurths. Coherence resonance in a noise-driven excitable system. *Phys. Rev. Lett.*, 78, 775, 1997.
32. J. García-Ojalvo and J. M. Sancho. Noise in Spatially Extended Systems. Springer, New York, 1999.
33. C. Masoller. Noise-induced resonance in delayed feedback systems. *Phys. Rev. Lett.*, 88, 034102, 2002.
34. B. Lindner, J. García-Ojalvo, A. Neiman, and L. Schimansky-Geier. Effects of noise in excitable systems. *Phys. Rep.*, 392, 321, 2004.
35. F. Sagués, J. M. Sancho, and J. García-Ojalvo. Spatiotemporal order out of noise. *Rev. Mod. Phys.*, 79, 829, 2007.
36. D. J. Gauthier, D. K. Sukow, H. M. Concannon, and J. E. S. Socolar. Stabilizing unstable periodic orbits in a fast diode resonator using continuous time-delay autosynchronization. *Phys. Rev. E*, 50, 2343, 1994.
37. J. N. Blakely, L. Illing, and D. J. Gauthier. Controlling fast chaos in delay dynamical systems. *Phys. Rev. Lett.*, 92, 193901, 2004.
38. S. Schikora, P. Hövel, H. J. Wünsche, E. Schöll, and F. Henneberger. All-optical noninvasive control of unstable steady states in a semiconductor laser. *Phys. Rev. Lett.*, 97, 213902, 2006.
39. J. E. S. Socolar, D. W. Sukow, and D. J. Gauthier. Stabilizing unstable periodic orbits in fast dynamical systems. *Phys. Rev. E*, 50, 3245, 1994.
40. J. E. S. Socolar and D. J. Gauthier. Analysis and comparison of multiple-delay schemes for controlling unstable fixed points of discrete maps. *Phys. Rev. E*, 57, 6589, 1998.
41. I. Harrington and J. E. S. Socolar. Design and robustness of delayed feedback controllers for discrete systems. *Phys. Rev. E*, 69, 056207, 2004.
42. M. E. Bleich and J. E. S. Socolar. Stability of periodic orbits controlled by time-delay feedback. *Phys. Lett. A*, 210, 87, 1996.
43. W. Just, T. Bernard, M. Ostheimer, E. Reibold, and H. Benner. Mechanism of time-delayed feedback control. *Phys. Rev. Lett.*, 78, 203, 1997.
44. H. Nakajima. On analytical properties of delayed feedback control of chaos. *Phys. Lett. A*, 232, 207, 1997.

45. K. Pyragas. Analytical properties and optimization of time-delayed feedback control. *Phys. Rev. E*, 66, 26207, 2002.
46. W. Just, H. Benner, and E. Schöll. Control of chaos by time–delayed feedback: a survey of theoretical and experimental aspects. In: B. Kramer (ed.), *Advances in Solid State Physics*. Springer, Berlin, 2003, vol. 43, pp. 589–603.
47. P. Hövel and J. E. S. Socolar. Stability domains for time-delay feedback control with latency. *Phys. Rev. E*, 68, 036206, 2003.
48. P. Hövel and E. Schöll. Control of unstable steady states by time-delayed feedback methods. *Phys. Rev. E*, 72, 046203, 2005.
49. S. Yanchuk, M. Wolfrum, P. Hövel, and E. Schöll. Control of unstable steady states by long delay feedback. *Phys. Rev. E*, 74, 026201, 2006.
50. T. Dahms, P. Hövel, and E. Schöll. Control of unstable steady states by extended time-delayed feedback. *Phys. Rev. E*, 76, 056201, 2007.
51. A. Amann, E. Schöll, and W. Just. Some basic remarks on eigenmode expansions of time-delay dynamics. *Physica A*, 373, 191, 2007.
52. B. Fiedler, V. Flunkert, M. Georgi, P. Hövel, and E. Schöll. Refuting the odd number limitation of time-delayed feedback control. *Phys. Rev. Lett.*, 98, 114101, 2007.
53. W. Just, B. Fiedler, V. Flunkert, M. Georgi, P. Hövel, and E. Schöll. Beyond odd number limitation: a bifurcation analysis of time-delayed feedback control. *Phys. Rev. E*, 76, 026210, 2007.
54. B. Fiedler, S. Yanchuk, V. Flunkert, P. Hövel, H. J. Wünsche, and E. Schöll. Delay stabilization of rotating waves near fold bifurcation and application to all-optical control of a semiconductor laser. *Phys. Rev. E*, 77, 066207, 2008.
55. A. G. Balanov, N. B. Janson, and E. Schöll. Delayed feedback control of chaos: Bifurcation analysis. *Phys. Rev. E*, 71, 016222, 2005.
56. J. Hizanidis, R. Aust, and E. Schöll. Delay-induced multistability near a global bifurcation. *Int. J. Bifur. Chaos*, 18, 1759, 2008.
57. K. Pyragas. Control of chaos via extended delay feedback. *Phys. Lett. A*, 206, 323, 1995.
58. A. Ahlborn and U. Parlitz. Stabilizing unstable steady states using multiple delay feedback control. *Phys. Rev. Lett.*, 93, 264101, 2004.
59. A. Ahlborn and U. Parlitz. Controlling dynamical systems using multiple delay feedback control. *Phys. Rev. E*, 72, 016206, 2005.
60. A. Gjurchinovski and V. Urumov. Stabilization of unstable steady states by variable delay feedback control. *Europhys. Lett.*, 84, 40013, 2008.
61. E. Schöll. Delayed feedback control of chaotic spatio-temporal patterns in semiconductor nanostructures. In: E. Schöll and H. G. Schuster (eds), [1], chap. 24, pp. 533–558, second completely revised and enlarged edition.
62. E. Schöll. Pattern formation and time-delayed feedback control at the nano-scale. In: G. Radons, B. Rumpf, and H. G. Schuster (eds.), *Nonlinear Dynamics of Nanosystems*. Wiley-VCH, Weinheim, 2009, pp. 325–367.
63. A. S. Mikhailov and K. Showalter. Control of waves, patterns and turbulence in chemical systems. *Phys. Rep.*, 425, 79, 2006.
64. P. Parmananda, R. Madrigal, M. Rivera, L. Nyikos, I. Z. Kiss, and V. Gáspár. Stabilization of unstable steady states and periodic orbits in an electrochemical system using delayed-feedback control. *Phys. Rev. E*, 59, 5266, 1999.
65. P. Parmananda. Tracking fixed-point dynamics in an electrochemical system using delayed-feedback control. *Phys. Rev. E*, 67, 045202R, 2003.
66. D. Battogtokh and A. S. Mikhailov. Controlling turbulence in the complex Ginzburg-Landau equation. *Physica D*, 90, 84, 1996.
67. J. Schlesner, V. Zykov, H. Engel, and E. Schöll. Stabilization of unstable rigid rotation of spiral waves in excitable media. *Phys. Rev. E*, 74, 046215, 2006.
68. G. J. E. Santos, J. Escalona, and P. Parmananda. Regulating noise-induced spiking using feedback. *Phys. Rev. E*, 73, 042102, 2006.

69. I. Z. Kiss, C. G. Rusin, H. Kori, and J. L. Hudson. Engineering Complex Dynamical Structures: Sequential Patterns and Desynchronization. *Science*, 316, 1886, 2007.
70. Y. Zhai, I. Z. Kiss, and J. L. Hudson. Control of complex dynamics with time-delayed feedback in populations of chemical oscillators: Desynchronization and clustering. *Ind. Eng. Chem. Res.*, 47, 3502, 2008.
71. M. G. Rosenblum and A. Pikovsky. Controlling synchronization in an ensemble of globally coupled oscillators. *Phys. Rev. Lett.*, 92, 114102, 2004.
72. O. V. Popovych, C. Hauptmann, and P. A. Tass. Effective desynchronization by nonlinear delayed feedback. *Phys. Rev. Lett.*, 94, 164102, 2005.
73. K. Hall, D. J. Christini, M. Tremblay, J. J. Collins, L. Glass, and J. Billette. Dynamic control of cardiac alterans. *Phys. Rev. Lett.*, 78, 4518, 1997.
74. F. M. Atay. Distributed delays facilitate amplitude death of coupled oscillators. *Phys. Rev. Lett.*, 91, 094101, 2003.
75. H. Haken. *Brain Dynamics: Synchronization and Activity Patterns in Pulse-Coupled Neural Nets with Delays and Noise*. Springer Verlag GmbH, Berlin, 2006.
76. K. Pyragas, O. V. Popovych, and P. A. Tass. Controlling synchrony in oscillatory networks with a separate stimulation-registration setup. *Europhys. Lett.*, 80, 40002, 2007.
77. M. Gassel, E. Glatt, and F. Kaiser. Time-delayed feedback in a net of neural elements: Transitions from oscillatory to excitable dynamics. *Fluct. Noise Lett.*, 7, L225, 2007.
78. M. Gassel, E. Glatt, and F. Kaiser. Delay-sustained pattern formation in subexcitable media. *Phys. Rev. E*, 77, 066220, 2008.
79. O. D'Huys, R. Vicente, T. Erneux, J. Danckaert, and I. Fischer. Synchronization properties of network motifs: Influence of coupling delay and symmetry. *Chaos*, 18, 037116, 2008.
80. G. C. Sethia, A. Sen, and F. M. Atay. Clustered chimera states in delay-coupled oscillator systems. *Phys. Rev. Lett.*, 100, 144102, 2008.
81. W. Kinzel, J. Kestler, and I. Kanter. *Chaos pass filter: Linear response of synchronized chaotic systems*. 2008. http://arxiv.org/abs/0806.4291
82. M. Zigzag, M. Butkovski, A. Englert, W. Kinzel, and I. Kanter. Zero-lag synchronization of chaotic units with time-delayed couplings. *Europhys. Lett.*, 85, 60005, 2009.
83. E. Schöll and K. Pyragas. Tunable semiconductor oscillator based on self-control of chaos in the dynamic Hall effect. *Europhys. Lett.*, 24, 159, 1993.
84. D. Reznik and E. Schöll. Oscillation modes, transient chaos and its control in a modulation-doped semiconductor double-heterostructure. *Z. Phys. B*, 91, 309, 1993.
85. D. P. Cooper and E. Schöll. Tunable real space transfer oscillator by delayed feedback control of chaos. *Z. f. Naturforsch.*, 50a, 117, 1995.
86. W. Just, S. Popovich, A. Amann, N. Baba, and E. Schöll. Improvement of time–delayed feedback control by periodic modulation: Analytical theory of Floquet mode control scheme. *Phys. Rev. E*, 67, 026222, 2003.
87. E. Schöll, A. G. Balanov, N. B. Janson, and A. Neiman. Controlling stochastic oscillations close to a Hopf bifurcation by time-delayed feedback. *Stoch. Dyn.*, 5, 281, 2005.
88. J. Pomplun, A. G. Balanov, and E. Schöll. Long-term correlations in stochastic systems with extended time-delayed feedback. *Phys. Rev. E*, 75, 040101(R), 2007.
89. T. Prager, H. P. Lerch, L. Schimansky-Geier, and E. Schöll. Increase of coherence in excitable systems by delayed feedback. *J. Phys. A*, 40, 11045, 2007.
90. A. Pototsky and N. B. Janson. Correlation theory of delayed feedback in stochastic systems below Andronov-Hopf bifurcation. *Phys. Rev. E*, 76, 056208, 2007.
91. A. Pototsky and N. B. Janson. Excitable systems with noise and delay, with applications to control: Renewal theory approach. *Phys. Rev. E*, 77, 031113, 2008.
92. A. G. Balanov, V. Beato, N. B. Janson, H. Engel, and E. Schöll. Delayed feedback control of noise-induced patterns in excitable media. *Phys. Rev. E*, 74, 016214, 2006.
93. B. Hauschildt, N. B. Janson, A. G. Balanov, and E. Schöll. Noise-induced cooperative dynamics and its control in coupled neuron models. *Phys. Rev. E*, 74, 051906, 2006.
94. E. Schöll, G. Hiller, P. Hövel, and M. A. Dahlem. Time-delayed feedback in neurosystems. *Phil. Trans. R. Soc. A*, 367, 1079, 2009.

95. V. Flunkert and E. Schöll. Suppressing noise-induced intensity pulsations in semiconductor lasers by means of time-delayed feedback. *Phys. Rev. E*, 76, 066202, 2007.
96. J. Hizanidis, A. G. Balanov, A. Amann, and E. Schöll. Noise-induced oscillations and their control in semiconductor superlattices. *Int. J. Bifur. Chaos*, 16, 1701, 2006.
97. J. Hizanidis, A. G. Balanov, A. Amann, and E. Schöll. Noise-induced front motion: signature of a global bifurcation. *Phys. Rev. Lett.*, 96, 244104, 2006.
98. J. Hizanidis and E. Schöll. Control of noise-induced spatiotemporal patterns in superlattices. *phys. stat. sol. (c)*, 5, 207, 2008.
99. J. Hizanidis and E. Schöll. Control of coherence resonance in semiconductor superlattices. *Phys. Rev. E*, 78, 066205, 2008.
100. G. Stegemann, A. G. Balanov, and E. Schöll. Delayed feedback control of stochastic spatiotemporal dynamics in a resonant tunneling diode. *Phys. Rev. E*, 73, 016203, 2006.
101. E. Schöll, N. Majer, and G. Stegemann. Extended time delayed feedback control of stochastic dynamics in a resonant tunneling diode. *phys. stat. sol. (c)*, 5, 194, 2008.
102. N. Majer and E. Schöll. Resonant control of stochastic spatio-temporal dynamics in a tunnel diode by multiple time delayed feedback. *Phys. Rev. E*, 79, 011109, 2009.
103. K. Pyragas, V. Pyragas, I. Z. Kiss, and J. L. Hudson. Stabilizing and tracking unknown steady states of dynamical systems. *Phys. Rev. Lett.*, 89, 244103, 2002.
104. S. Bielawski, M. Bouazaoui, D. Derozier, and P. Glorieux. Stabilization and characterization of unstable steady states in a laser. *Phys. Rev. A*, 47, 3276, 1993.
105. A. Chang, J. C. Bienfang, G. M. Hall, J. R. Gardner, and D. J. Gauthier. Stabilizing unstable steady states using extended time-delay autosynchronisation. *Chaos*, 8, 782, 1998.
106. K. Pyragas, V. Pyragas, I. Z. Kiss, and J. L. Hudson. Adaptive control of unknown unstable steady states of dynamical systems. *Phys. Rev. E*, 70, 026215, 2004.
107. E. M. Wright. The linear difference-differential equation with constant coefficients. *Proc. R. Soc. Edinburgh, Sect. A: Math. Phys. Sci.*, 62, 387, 1949.
108. E. M. Wright. A non-linear difference-differential equation. *J. Reine Angew. Math.*, 194, 66, 1955.
109. R. Bellmann and K. L. Cooke. *Differential-Difference Equations*. Academic Press, New York, 1963.
110. J. K. Hale. *Functional Differential Equations*. Applied Mathematical Sciences Vol. 3, Springer, New York, 1971.
111. F. M. Asl and A. G. Ulsoy. Analysis of a system of linear delay differential equations. *ASME J. Dyn. Syst., Meas., Control*, 125, 215, 2003.
112. W. Just, E. Reibold, H. Benner, K. Kacperski, P. Fronczak, and J. Holyst. Limits of time-delayed feedback control. *Phys. Lett. A*, 254, 158, 1999.
113. S. Yanchuk and M. Wolfrum. Instabilities of equilibria of delay-differential equations with large delay. In: *Proc. 5th EUROMECH Nonlinear Dynamics Conference ENOC-2005, Eindhoven*, edited by D. H. van Campen, M. D. Lazurko, and W. P. J. M. van den Oever (Eindhoven University of Technology, Eindhoven, Netherlands, 2005), pp. 08–010, eNOC Eindhoven (CD ROM), ISBN 90 386 2667 3.
114. S. Lepri, G. Giacomelli, A. Politi, and F. T. Arecchi. High-dimensional chaos in delayed dynamical-systems. *Physica D*, 70, 235, 1994.
115. K. Pyragas and A. Tamaševičius. Experimental control of chaos by delayed self-controlling feedback. *Phys. Lett. A*, 180, 99, 1993.
116. S. Bielawski, D. Derozier, and P. Glorieux. Controlling unstable periodic orbits by a delayed continuous feedback. *Phys. Rev. E*, 49, R971, 1994.
117. T. Pierre, G. Bonhomme, and A. Atipo. Controlling the chaotic regime of nonlinear ionization waves using time-delay autosynchronisation method. *Phys. Rev. Lett.*, 76, 2290, 1996.
118. D. W. Sukow, M. E. Bleich, D. J. Gauthier, and J. E. S. Socolar. Controlling chaos in a fast diode resonator using time-delay autosynchronisation: Experimental observations and theoretical analysis. *Chaos*, 7, 560, 1997.
119. O. Lüthje, S. Wolff, and G. Pfister. Control of chaotic taylor-couette flow with time-delayed feedback. *Phys. Rev. Lett.*, 86, 1745, 2001.

120. J. M. Krodkiewski and J. S. Faragher. Stabilization of motion of helicopter rotor blades using delayed feedback - modelling, computer simulation and experimental verification. *J. Sound Vib.*, 234, 591, 2000.
121. T. Fukuyama, H. Shirahama, and Y. Kawai. Dynamical control of the chaotic state of the current-driven ion acoustic instability in a laboratory plasma using delayed feedback. *Phys. Plasmas*, 9, 4525, 2002.
122. C. von Loewenich, H. Benner, and W. Just. Experimental relevance of global properties of time-delayed feedback control. *Phys. Rev. Lett.*, 93, 174101, 2004.
123. H. Nakajima and Y. Ueda. Limitation of generalized delayed feedback control. *Physica D*, 111, 143, 1998.
124. I. Harrington and J. E. S. Socolar. Limitation on stabilizing plane waves via time-delay feedback. *Phys. Rev. E*, 64, 056206, 2001.
125. K. Pyragas, V. Pyragas, and H. Benner. Delayed feedback control of dynamical systems at subcritical Hopf bifurcation. *Phys. Rev. E*, 70, 056222, 2004.
126. V. Pyragas and K. Pyragas. Delayed feedback control of the Lorenz system: An analytical treatment at a subcritical Hopf bifurcation. *Phys. Rev. E*, 73, 036215, 2006.
127. H. G. Schuster and M. B. Stemmler. Control of chaos by oscillating feedback. *Phys. Rev. E*, 56, 6410, 1997.
128. H. Nakajima and Y. Ueda. Half-period delayed feedback control for dynamical systems with symmetries. *Phys. Rev. E*, 58, 1757, 1998.
129. K. Pyragas. Control of chaos via an unstable delayed feedback controller. *Phys. Rev. Lett.*, 86, 2265, 2001.
130. B. Fiedler, V. Flunkert, M. Georgi, P. Hövel, and E. Schöll. Beyond the odd number limitation of time-delayed feedback control. In: E. Schöll and H. G. Schuster (eds.), *Handbook of Chaos Control*. Wiley-VCH, Weinheim, 2008, pp. 73–84, second completely revised and enlarged edition.
131. O. Diekmann, S. A. van Gils, S. M. Verduyn Lunel, and H. O. Walther. *Delay Equations*. Springer-Verlag, New York, 1995.
132. Y. A. Kuznetsov. *Elements of Applied Bifurcation Theory*. Springer, New York, 1995.
133. Z. Gills, C. Iwata, R. Roy, I. B. Schwartz, and I. Triandaf. Tracking unstable steady states: Extending the stability regime of a multimode laser system. *Phys. Rev. Lett.*, 69, 3169, 1992.
134. A. Ahlborn and U. Parlitz. Chaos control using notch feedback. *Phys. Rev. Lett.*, 96, 034102, 2006.
135. S. Bauer, O. Brox, J. Kreissl, B. Sartorius, M. Radziunas, J. Sieber, H. J. Wünsche, and F. Henneberger. Nonlinear dynamics of semiconductor lasers with active optical feedback. *Phys. Rev. E*, 69, 016206, 2004.
136. H. J. Wünsche, S. Bauer, J. Kreissl, O. Ushakov, N. Korneyev, F. Henneberger, E. Wille, H. Erzgräber, M. Peil, W. Elsäßer, and I. Fischer. Synchronization of delay-coupled oscillators: A study of semiconductor lasers. *Phys. Rev. Lett.*, 94, 163901, 2005.
137. W. Lu and R. G. Harrison. Controlling chaos using continuous interference feedback: proposal for all optical devices. *Opt. Commu.*, 109, 457, 1994.
138. C. Simmendinger and O. Hess. Controlling delay-induced chaotic behavior of a semiconductor laser with optical feedback. *Phys. Lett. A*, 216, 97, 1996.
139. V. Z. Tronciu, H. J. Wünsche, M. Wolfrum, and M. Radziunas. Semiconductor laser under resonant feedback from a Fabry-Perot: Stability of continuous-wave operation. *Phys. Rev. E*, 73, 046205, 2006.
140. B. Dahmani, L. Hollberg, and R. Drullinger. Frequency stabilization of semiconductor lasers by resonant optical feedback. *Opt. Lett.*, 12, 876, 1987.
141. P. Laurent, A. Clairon, and C. Breant. Frequency noise analysis of optically self-locked diode lasers. *IEEE J. Quantum Electron.*, 25, 1131, 1989.
142. M. Peil, I. Fischer, and W. Elsäßer. Spectral braodband dynamics of seminconductor lasers with resonant short cavities. *Phys. Rev. A*, 73, 23805, 2006.

143. H. Erzgräber, B. Krauskopf, D. Lenstra, A. P. A. Fischer, and G. Vemuri. Frequency versus relaxation oscillations in a semiconductor laser with coherent filtered optical feedback. *Phys. Rev. E*, 73, 055201(R), 2006.
144. T. Dahms, P. Hövel, and E. Schöll. Stabilizing continuous-wave output in semiconductor lasers by time-delayed feedback. *Phys. Rev. E*, 78, 056213, 2008.
145. M. G. Rosenblum and A. Pikovsky. Delayed feedback control of collective synchrony: An approach to suppression of pathological brain rhythms. *Phys. Rev. E*, 70, 041904, 2004.
146. H. J. Wünsche, S. Schikora, and F. Henneberger. Noninvasive control of semiconductor lasers by delayed optical feedback. In: E. Schöll and H. G. Schuster (eds.), *Handbook of Chaos Control*. Wiley-VCH, Weinheim, 2008, second completely revised and enlarged edition.
147. R. Lang and K. Kobayashi. External optical feedback effects on semiconductor injection laser properties. *IEEE J. Quantum Electron*, 16, 347, 1980.
148. G. P. Agrawal and G. R. Gray. Effect of phase-conjugate feedback on the noise characteristics of semiconductor-lasers. *Phys. Rev. A*, 46, 5890, 1992.
149. P. M. Alsing, V. Kovanis, A. Gavrielides, and T. Erneux. Lang and Kobayashi phase equation. *Phys. Rev. A*, 53, 4429, 1996.
150. G. P. Agrawal and N. K. Dutta. *Semiconductor Lasers*. Van Nostrand Reinhold, New York, 1993.
151. R. FitzHugh. Impulses and physiological states in theoretical models of nerve membrane. *Biophys. J.*, 1, 445, 1961.
152. J. Nagumo, S. Arimoto, and S. Yoshizawa. An active pulse transmission line simulating nerve axon. *Proc. IRE*, 50, 2061, 1962.
153. P. Hövel, M. A. Dahlem, and E. Schöll. Control of synchronization in coupled neural systems by time-delayed feedback. *Int. J. Bifur. Chaos*, 2010, in print (arxiv:0809.0819v1).
154. M. A. Dahlem, G. Hiller, A. Panchuk, and E. Schöll. Dynamics of delay-coupled excitable neural systems. *Int. J. Bifur. Chaos*, 19, 745, 2009.
155. D. Schmitz, S. Schuchmann, A. Fisahn, A. Draguhn, E. H. Buhl, E. Petrasch-Parwez, R. Dermietzel, U. Heinemann, and R. D. Traub. Axo-axonal coupling. a novel mechanism for ultrafast neuronal communication. *Neuron*, 31, 831, 2001.
156. D. T. J. Liley and J. J. Wright. Intracortical connectivity of pyramidal and stellate cells: estimates of synaptic densities and coupling symmetry. *Network: Comput. Neural Syst.*, V5, 175, 1994.
157. R. D. Pinto, P. Varona, A. R. Volkovskii, A. Szücs, H. D. I. Abarbanel, and M. I. Rabinovich. Synchronous behavior of two coupled electronic neurons. *Phys. Rev. E*, 62, 2644, 2000.
158. F. F. De-Miguel, M. Vargas-Caballero, and E. García-Pérez. Spread of synaptic potentials through electrical synapses in Retzius neurones of the leech. *J. Exp. Biol.*, 204, 3241, 2001.
159. N. Buric and D. Todorovic. Dynamics of FitzHugh-Nagumo excitable systems with delayed coupling. *Phys. Rev. E*, 67, 066222, 2003.
160. V. Hadamschek. Brain stimulation techniques via nonlinear delayed neurofeedback based on MEG inverse methods. PhD Thesis, TU Berlin, 2006.
161. P. Tass. Effective desynchronization with bipolar double-pulse stimulation. *Phys. Rev. E*, 66, 036226, 2002.
162. M. G. Rosenblum, A. Pikovsky, and J. Kurths. *Synchronization – A universal concept in nonlinear sciences*. Cambridge University Press, Cambridge, 2001.